AN *AB INITIO* INVESTIGATION OF STRUCTURE-FUNCTION RELATIONSHIPS IN SOLID-STATE ELECTROLYTES

A Thesis

Presented to

the Faculty of the Department of Electrical and Computer Engineering

and the Department of Chemical and Biomolecular Engineering

University of Houston

In Partial Fulfillment

of the Requirements for the Degree

Bachelor of Science

in Electrical Engineering

by Audrey Elyse Wang

May 2019

AN *AB INITIO* INVESTIGATION OF STRUCTURE-FUNCTION RELATIONSHIPS

IN SOLID-STATE ELECTROLYTES

Audrey Elyse Wang

Approved:

Yan Yao, Ph.D.
Chair of the Committee
Department of Electrical and Computer Engineering

Committee Members:

Lars Grabow, Ph.D.
Department of Chemical and Biomolecular Engineering

Fritz Claydon, Ph.D.
Department of Electrical and Computer Engineering
The Honors College

Suresh K. Khator, Associate Dean
Cullen College of Engineering

Badri Roysam, Ph.D. and Chair
Department of Electrical and Computer Engineering

Acknowledgments

First and foremost, I would like to thank Professor Yan Yao for giving me the opportunity to venture out of electrical engineering and into the realm of materials science and electrochemistry. Through this experience studying battery materials, I have discovered that energy storage is a passion of mine that I will continue to pursue throughout my career.

I would also like to thank Professor Lars Grabow and the rest of the UH Computational Catalysis and Interface Chemistry Group for welcoming me into the group and for their invaluable expertise regarding density functional theory. It was my absolute pleasure to work with such joyful and supportive colleagues and friends.

I am also thankful for Professor Fritz Claydon and the mentorship he has provided to me since my first year at the University of Houston. His belief in me as a freshman helped me to build confidence in my own abilities and to accomplish far more in my undergraduate career than I ever imagined.

My sincere thanks also go out to Karun Kumar Rao, without whom my completion of this research project would have been impossible. Karun coached me and challenged me, and for his guidance, I am deeply grateful.

Finally, I want to thank my parents for fostering my dream of becoming an engineer since I was a child and my fiancé for always being available to be my sounding board and for being an unwavering source of strength and motivation.

An *Ab Initio* Investigation of Structure-Function Relationships in Solid-State Electrolytes

An Abstract

of a

Thesis

Presented to

the Faculty of the Department of Electrical and Computer Engineering

and the Department of Chemical and Biomolecular Engineering

University of Houston

In Partial Fulfillment

of the Requirements for the Degree

Bachelor of Science

in Electrical Engineering

by Audrey Elyse Wang

May 2019

Abstract

Solid-state electrolytes (SSEs), or superionic conductors, are a promising method of energy storage and a safer alternative to conventional Li-ion batteries. However, the ionic conductivities of most known SSEs, a characteristic integral to battery performance, are not yet commercially competitive. Ionic conductivity in SSEs is often achieved through the interstitial hopping of the mobile cation, so understanding the energetics of the crystal structure is important. The objective of this thesis is to use density function theory (DFT) to investigate the relationships between crystal structure and ionic conductivity of SSEs. Activation energies were calculated using DFT and nudged elastic band theory for sulfide and oxide frameworks with either lithium or sodium cations. The energy pathways generated in this study were consistent with previous findings that materials with BCC structures have the lowest energy barriers and thus have the highest ionic conductivities due to their homogenous tetrahedral sites.

Table of Contents

Acknowledgments iv

Abstract vi

Table of Contents vii

List of Figures ix

Chapter One – Introduction 1

1.1 Motivation for Studying Battery Energy Storage Systems 1

1.2 Ion Transport in Batteries 4

1.3 Using Density Functional Theory to Investigate Ionic Conductivity 6

1.4 Project Statement & Scope 9

Chapter Two – Methods 10

2.1 Selecting Crystal Structures 10

2.2 Interstitial Sites and Ion Hopping Paths 11

2.3 DFT Workflow 13

2.4 Nudged Elastic Band Calculations 15

Chapter Three – Results & Discussion 16

3.1 Lithium Cations in a Sulfide Framework (Li-S) 16

3.1.1 Li-S Body-Centered Cubic 16

3.1.2 Li-S Face Centered Cubic 17

3.1.3 Li-S Hexagonal Close Packing 18

3.1.4 Activation Energy for Li-ion Migration in S Anion Framework vs. Volume 21

3.2 Sodium Cations in a Sulfide Framework (Na-S) 23

3.2.1 Na-S Body-Centered Cubic 23

3.2.2 Na-S Face-Centered Cubic.....24

3.2.3 Na-S Hexagonal Close Packing.....25

3.2.4 Activation Energy for Na-ion Migration in S Anion Framework vs. Volume.....26

3.3 Lithium Cations in an Oxide Framework (Li-O) 27

3.3.1 Li-O Body-Centered Cubic.....27

3.3.2 Li-O Face-Centered Cubic.....28

3.3.3 Li-O Hexagonal Close Packing 28

3.3.4 Activation Energy for Li-ion Migration in O Anion Framework vs. Volume.....30

3.4 Sodium Cations in an Oxide Framework (Na-O) 31

3.4.1 Na-O Body-Centered Cubic 31

3.4.2 Na-O Face-Centered Cubic 32

3.4.4 Activation Energy for Na-ion Migration in O Anion Framework vs. Volume 34

3.5 Limitations of Current Results.....34

Chapter Four – Summary and Conclusions 35

References 38

Appendix 41

List of Figures

Figure 1. High-level overview of how ions and electrons move in lithium-ion batteries.....2

Figure 2. Tetrahedral and an octahedral interstitial site. The tetrahedral site (a) has four anions around a cation, and the octahedral site (b) has six anions around a cation. Anions in blue, cations in gold. 4

Figure 3. High-level overview of the algorithm used for DFT energy relaxations. Note that $Fi - Fi - 1 < Fcutoff$ means the forces of the previous iteration $(i - 1)$ subtracted from the current iteration i must be below a specified cutoff value. 7

Figure 4. Crystal structure models and energy landscape plots from "Design principles for solid-state lithium superionic conductors" by Wang *et al.* for BCC, FCC, and HCP crystal structures composed of a sulfur anion lattice (yellow) and Li-ion charge carriers (green) [6]. 8

Figure 5. Anion sublattice mapping. a) Existing superionic conductor $Li_{10}GeP_2S_{12}$ (LGPS) [12]. b) LGPS with Ge (blue) and P (green) removed. c) LGPS ultimately maps closely to a single bcc unit cell of sulfur anions with one lithium ion in a tetrahedral site [13]. Sulfur anions in yellow, Li-ions in purple. 9

Figure 6. Li-ion migration between tetrahedral sites T1 and T2 in a primitive BCC sulfur cell. 11

Figure 7. Li-ion migration from tetrahedral site T1 to octahedral site O1 and finally to tetrahedral site T2 in a primitive FCC sulfur cell.....12

Figure 8. Li-ion migration in a primitive HCP sulfur cell. There are three paths for ionic interstitial hopping: tetrahedral to tetrahedral (T1-T3), tetrahedral to octahedral to tetrahedral (T1-O1-T2), and octahedral to octahedral (O1-O2). 12

Figure 9. Illustration of how VASP incorporates a uniform background charge.....14

Figure 10. Example of how an Li-ion migration path is interpolated for an NEB calculation. 15

Figure 11. Energy landscapes for a Li-ion migrating through a BCC S anion sublattice via a T-T path. 16

Figure 12. Findings from Wang *et al.* of the energy landscapes for a Li-ion migrating through a BCC S anion sublattice via a T-T path [6]. 16

Figure 13. Energy landscapes for a Li-ion migrating through an FCC S anion sublattice via a T-O-T path. 17

Figure 14. Findings from Wang *et al.* of the energy landscapes for a Li-ion migrating through an FCC S anion sublattice via a T-O-T path [6]. 18

Figure 15. Energy landscapes for a Li-ion migrating through an HCP S anion sublattice via a T-T path. 18

Figure 16. Findings from Wang *et al.* of the energy landscapes for a Li-ion migrating through an HCP S anion sublattice via a T-T path [6]. 19

Figure 17. Energy landscapes for a Li-ion migrating through an HCP S anion sublattice via an O-O path. 19

Figure 18. Findings from Wang *et al.* of the energy landscapes for a Li-ion migrating through an HCP S anion sublattice via an O-O path [6]. 20

Figure 19. Energy landscapes for a Li-ion migrating through an HCP S anion sublattice via a T-O-T path. 20

Figure 20. Findings from Wang *et al.* of the energy landscapes for a Li-ion migrating through an HCP S anion sublattice via a T-O-T path [6]. 21

Figure 21. Energy barriers versus cell volume per S anion for various Li-S crystal structures. The dotted lines show the expected trends. 22

Figure 22. Findings from previous work of the energy barriers versus cell volume per S anion for various Li-S crystal structures [6]. 23

Figure 23. Energy landscapes for a Na-ion migrating through a BCC S anion sublattice via a T-T path. 24

Figure 24. Energy landscapes for a Na-ion migrating through an FCC S anion sublattice via a T-O-T path. 24

Figure 25. Energy landscapes for a Na-ion migrating through an HCP S anion sublattice via a T-T path. 25

Figure 26. Energy landscapes for a Na-ion migrating through an HCP S anion sublattice via an O-O path. 26

Figure 27. Energy landscapes for a Na-ion migrating through an HCP S anion sublattice via a T-O-T path. 26

Figure 28. Energy barriers versus cell volume per S anion for various Na-S crystal structures. 27

Figure 29. Findings from Wang *et al.* of the energy barriers versus cell volume per S anion for various Na-S crystal structures [6]. 27

Figure 30. Energy landscapes for a Li-ion migrating through a BCC O anion sublattice via a T-T path. 28

Figure 31. Energy landscapes for a Li-ion migrating through an FCC O anion sublattice via a T-O-T path. 28

Figure 32. Energy landscapes for a Li-ion migrating through an HCP O anion sublattice via a T-T path. 29

Figure 33. Energy landscapes for a Li-ion migrating through an HCP O anion sublattice via an O-O path. 29

Figure 34. Energy landscapes for a Li-ion migrating through an HCP O anion sublattice via a T-O-T path. 30

Figure 35. Energy barriers versus cell volume per O anion for various Li-O crystal structures. 30

Figure 36. Findings from Wang *et al.* of the energy barriers versus cell volume per O anion for various Li-O crystal structures [6]. 31

Figure 37. Energy landscapes for a Na-ion migrating through a BCC O anion sublattice via a T-T path. 32

Figure 38. Energy landscapes for a Na-ion migrating through an FCC O anion sublattice via a T-O-T path. 32

Figure 39. Energy landscapes for a Na-ion migrating through an HCP O anion sublattice via a T-T path. 33

Figure 40. Energy landscapes for a Na-ion migrating through an HCP O anion sublattice via an O-O path. 33

Figure 41. Energy landscapes for a Na-ion migrating through an HCP O anion sublattice via a T-O-T path. 33

Figure 42. Energy barriers versus cell volume per O anion for various Na-O crystal structures. 34

Chapter One – Introduction

1.1 Motivation for Studying Battery Energy Storage Systems

It is well known that anthropogenic global climate change is drastically altering the planet. As the global population grows, the demand for energy, the excavation of non-renewable resources, and the production of carbon emissions also rise. Worldwide dependence on fossil fuels is clearly the primary factor behind climate change, so some of the main challenges of this century are transitioning global energy dependence to sustainable energy sources and starkly reducing energy consumption.

Two prominent strategies for increasing sustainability have emerged: first, generating electricity using renewable energy sources and, second, powering vehicles with sustainably generated electricity. However, the success of both renewable energy and electric vehicles (EVs) depends on energy storage development. In the case of renewable energy, the two frontrunners to replace traditional fossil fuels are wind and solar energy, but the sporadic nature of wind and sunlight render these sources unable to readily meet consumer needs. In fact, the rapid integration of renewable energy sources without supplementary storage systems could be catastrophic; it has been estimated that if renewables grow to constitute 20% or more of the power supply, then the grid will become destabilized [1]. Similarly, the marketability of electric vehicles depends entirely on the battery system capacity and cost. Therefore, developing high-capacity, cost-effective, and environmentally-sound energy storage systems is one of the most pressing issues in the engineering community.

Although no one energy storage device can fit all possible application requirements, Li-ion batteries are prime candidates to solve many of the world's storage needs. Being the most electropositive element and extremely lightweight, lithium makes for batteries with high voltages and high volumetric energy densities, which are especially desirable qualities for grid-

scale energy storage [2]. For EVs, rapid charge and discharge capabilities are necessary and can be made possible with Li-ion batteries due to the small radius, and thus fast diffusion, of lithium ions [2]. However, conventional Li-ion batteries suffer from high flammability as was seen in 2016 when Samsung Galaxy Note 7 phones exploded as a result of faulty Li-ion batteries. A failure on the grid- or vehicle-scale would be much more disastrous due to the large amount of energy being stored, so safety is a primary concern for battery development.

Batteries are energy storage devices that consist of an anode, a cathode, and an electrolyte, as seen in Figure 1. When a battery is connected to a circuit, a pair of redox reactions occurs on the anode and cathode. For example, in a lithium-ion battery, lithium deintercalates from the graphite anode to yield lithium cations and free electrons. Since the electrolyte is electronically insulating, the electrons travel externally through the circuit, providing electricity to the device, and the ions travel through the electrolyte, where they are reduced at the cathode.

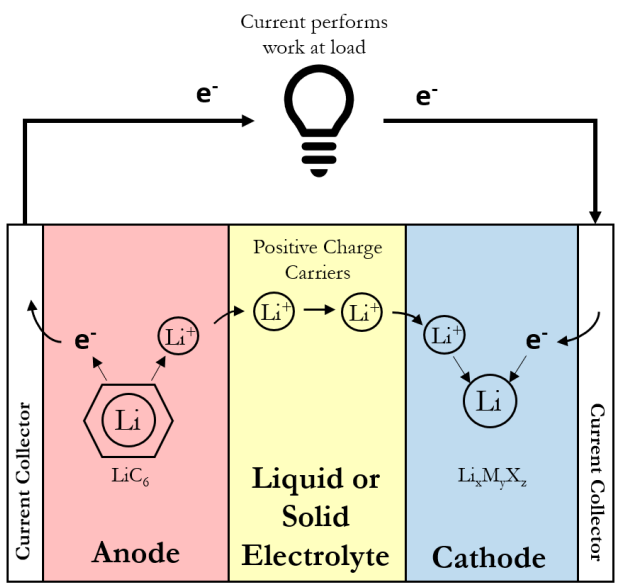

Figure 1. High-level overview of how ions and electrons move in lithium-ion batteries.

Generally speaking, battery performance is judged based on four main attributes: voltage, current capacity, energy density, and power density.

Voltage (V_{cell}) is the electric potential difference between the anode and the cathode, as shown in equation 1,

$$V_{cell} = E_{cathode} - E_{anode}, \tag{1}$$

where $E_{cathode}$ is the potential of the cathode, and E_{anode} is the potential of the anode [3]. As aforementioned, the electropositive nature of lithium contributes to the high voltages of Li-ion batteries. For applications such as grid-scale storage, it is ideal to use batteries with the highest voltage possible so that fewer cells are necessary [4].

Charge capacity (C_{cell}) is the amount of electric charge available in the battery, as shown in equation 2,

$$C_{cell} = (C_c^{-1} + C_a^{-1})^{-1}, \tag{2}$$

where C_c and C_a are the specific capacities of the cathode and anode, respectively [3]. The amount of available charge depends on the amount of materials in the battery [4].

Energy density (E_d) is the energy per total volume of the anode and cathode materials, as given by equation 3,

$$E_d = \frac{Energy}{Volume} = \frac{C_{cell} \times V_{cell} \times (W_c + W_a + W_e)}{\frac{W_c}{\rho_c} + \frac{W_a}{\rho_a} + \frac{W_e}{\rho_e}}, \tag{3}$$

where $W_{c/a/e}$ and $\rho_{c/a/e}$ are the weight and density of the cathode/anode/electrolyte, respectively [3].

Finally, the characteristic that this thesis will focus on is power density, the amount of power per unit volume [4]. Since power is defined as the product of voltage and current and the voltage of a battery is effectively constant, power density is determined by the amount of current that can be drawn from a battery (For the purposes of this thesis, current will be referred to as the flow of electrons).

For example, electric vehicles need batteries with high power density for rapid charge and discharge [5]. As illustrated by Figure 1, the speed of the electrons through the load is limited by the speed of their positive charge carrier counterparts through the battery's electrolyte. The system will maintain its charge neutrality, and therefore, the power that can be extracted from a battery depends on how quickly and easily positive ions can travel through the electrolyte, otherwise known as the ionic conductivity of the electrolyte.

1.2 Ion Transport in Batteries

Ions move through the electrolyte by hopping between interstitial sites [6]. Interstitial sites are the normally unoccupied spaces or vacancies in a crystal structure that are typically the most energetically stable. There are two varieties of interstitial sites that will be considered in this thesis: tetrahedral (T-site) and octahedral (O-site). A tetrahedral site is a vacancy that is formed by four atoms in the shape of a tetrahedron (Figure 2a), and similarly, an octahedral site is a vacancy that is formed by six atoms in the shape of an octahedron (Figure 2b). This thesis will show how the size and configuration of these interstitial sites determine the ionic conductivity of each crystal structure.

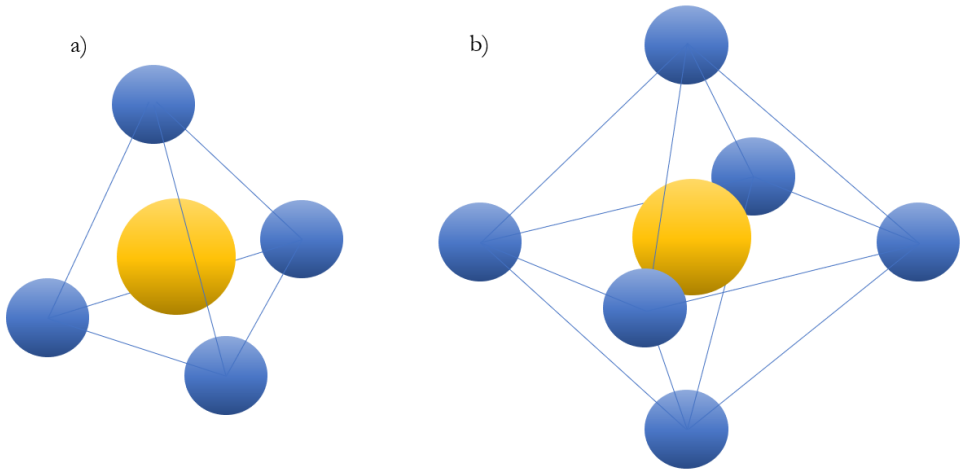

Figure 2. Tetrahedral and an octahedral interstitial site. The tetrahedral site (a) has four anions around a cation, and the octahedral site (b) has six anions around a cation. Anions in blue, cations in gold.

Conventional batteries contain liquid organic electrolytic solutions, and although they possess desirable ionic conductivities in the order of 1 [mS cm^{-1}], they are plagued by high flammability [6]. Conversely, electrolytes made of inorganic solid materials are of interest because they are electrochemically stable and not flammable [6]. The only solid-state battery that is presently viable on an industry level is a sodium-sulfur battery than can only be used at high temperatures (~250-300 [°C]) [7]. Clearly, solid-state electrolytes are hindered by generally low ionic conductivities and require further research and development, both experimental and computational, to become truly competitive with conventional liquid electrolytes.

That being said, several solid-state electrolytes have demonstrated remarkably high ionic conduction and are thusly known as "superionic conductors." Regarding Li-ion conductors, oxide-based superionic conductors have shown ionic conductivities in the range of 10^{-3} to 1 [mS cm^{-1}], and sulfide-based superionic conductors have shown ionic conductivities above 1 [mS cm^{-1}] [6]. These numbers are comparable to those of liquid electrolytes (in the range of 1 [mS cm^{-1}]) and bode well for the future commercialization of Li-ion solid-state electrolytes [6].

Lithium-ion technology will likely be the leader of the solid-state battery industry due to the exceptional mobility of Li-ions in many solids [8]. However, growing demand and possible scarcity of lithium has led to extreme price increases and narrowing profit margins for Li-ion battery manufacturers [9]. To combat the potential resource and cost issues of lithium, sodium-ion technologies are garnering interest because sodium is less expensive and much more abundant than lithium. It is worth noting that lithium's future in the battery industry is highly debated. While many believe that lithium will become too scarce and, consequently, too expensive, some studies suggest that there exist sufficient lithium reserves to maintain prices at reasonable levels [10]. Regardless, it is imperative to research tangentially lithium-ion technologies, which are clearly superior and promising in their performance abilities, as well

as other alternative materials like sodium that will be necessary for producing environmentally sustainable and cost-effective batteries, especially if the era of lithium wanes.

1.3 Using Density Functional Theory to Investigate Ionic Conductivity

The aim of this thesis is to investigate the relationship between ionic conductivity and crystal structure in solid-state electrolytes. This study of ionic conductivity is performed by analyzing the activation energy for each crystal structure as structural energy is linked to ionic conductivity through the relationship shown in equation 4,

$$\sigma = Ae^{\frac{-\Delta E}{k_b T}}, \tag{4}$$

where σ is ionic conductivity, ΔE is activation energy, T is temperature, A is the pre-exponential factor, and k_b is the Boltzmann constant. Physically, the activation energy is the energy needed for an ion to hop from one interstitial site to another (as shown in Figure 4), and mathematically, ionic conductivity increases as the activation energy of a crystal structure decreases (as shown in equation 1).

The activation energies of solid crystal structures can be determined via Density Functional Theory (DFT). Based on the Schrödinger Equation, DFT is a quantum approach for finding the ground-state energy of a crystal structure using its electron density [11]. For the scope of this project, a deep understanding of how DFT operates is not necessary. Figure 3 shows a general overview for how DFT energy relaxations are performed.

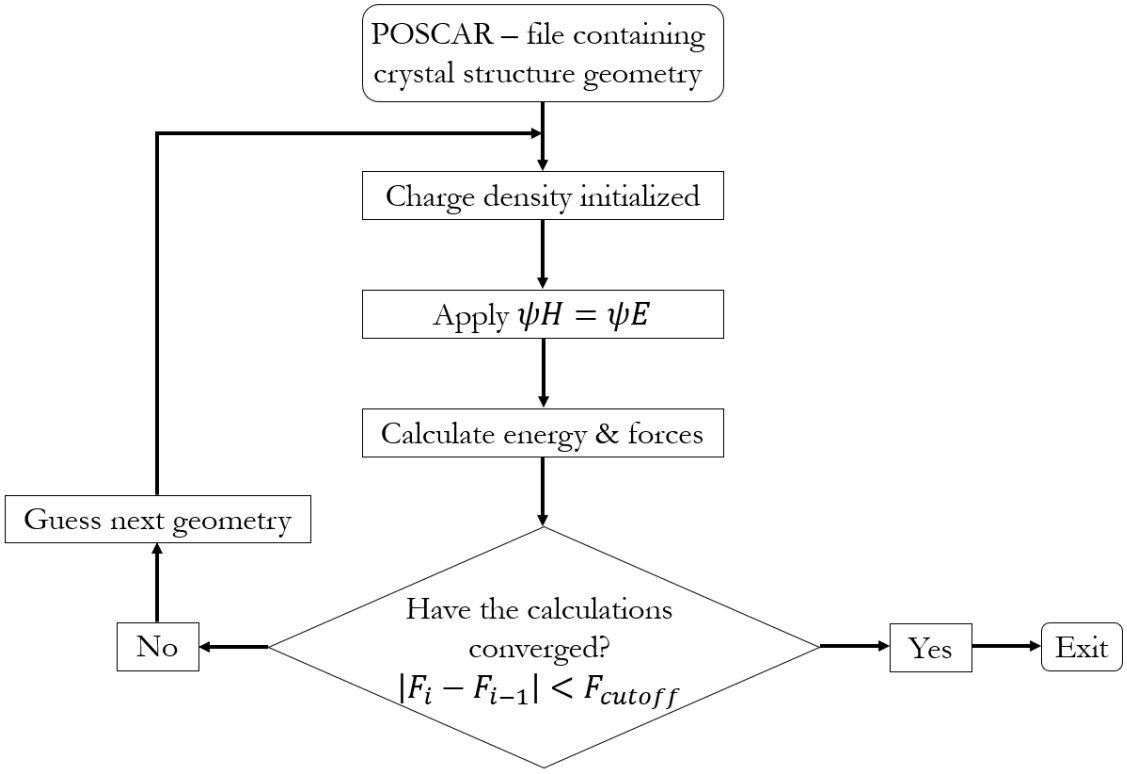

Figure 3. High-level overview of the algorithm used for DFT energy relaxations. Note that $|F_i - F_{i-1}| < F_{cutoff}$ means the forces of the previous iteration $(i-1)$ subtracted from the current iteration i must be below a specified cutoff value.

When combined with the Nudged Elastic Band (NEB) theory, DFT can be used to identify superionic conductors. The NEB method involves calculating the ground state energy of an ion at every point along its migration path through a solid crystal. For this thesis, NEB theory was applied to the path of a cation hopping between interstitial sites in an anion lattice to produce energy landscapes, examples of which are shown in the Li-ion migration plots from Figure 4. From these energy landscapes, the activation energy for each structure can be obtained (where ΔE is the largest change in energy for each plot), and thus, the ionic conductivity of each structure relative to the others can be determined.

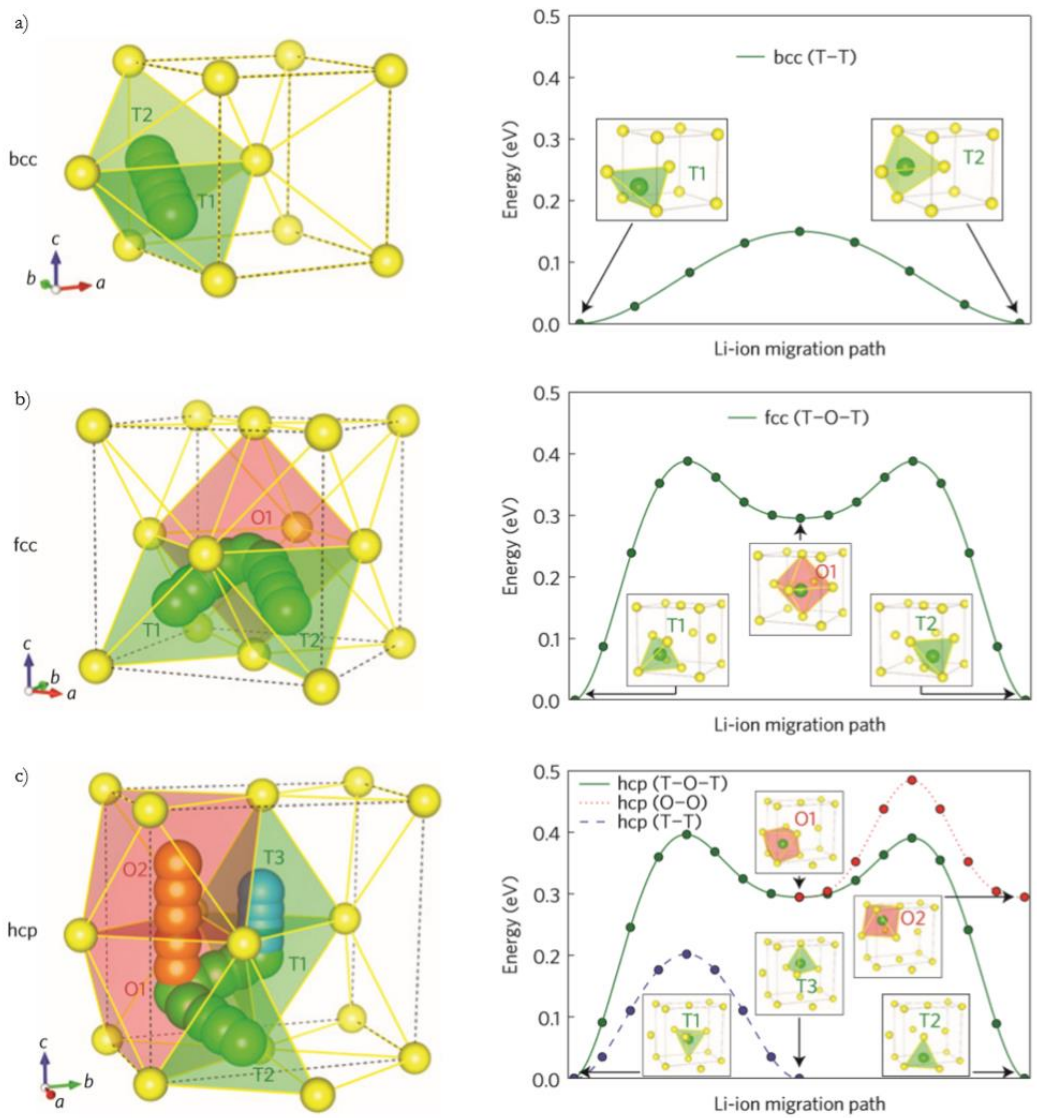

Figure 4. Crystal structure models and energy landscape plots from "Design principles for solid-state lithium superionic conductors" by Wang *et al.* for BCC, FCC, and HCP crystal structures composed of a sulfur anion lattice (yellow) and Li-ion charge carriers (green) [6].

In their 2015 paper "Design principles for solid-state lithium superionic conductors", Wang *et al.* used Density Functional Theory and Nudged Elastic Band theory to find a correlation between crystal structure and ionic conductivity. Their work is built on the premise that ionic conductivity is primarily linked to the shape of the anion sublattice of a material. This means that DFT calculations do not need to be performed on an accurate model of an actual existing material, which may be incredibly complex, but rather on a simplified model of

the structure that only contains an anion framework and mobile cations. Figure 5 shows how $Li_{10}GeP_2S_{12}$, an existing superionic conductor, is mapped to a simplified anion sublattice model. Because DFT calculations require expensive high-performance computing power, simplifying models is cost- and time-effective and limits the number of variables in a system.

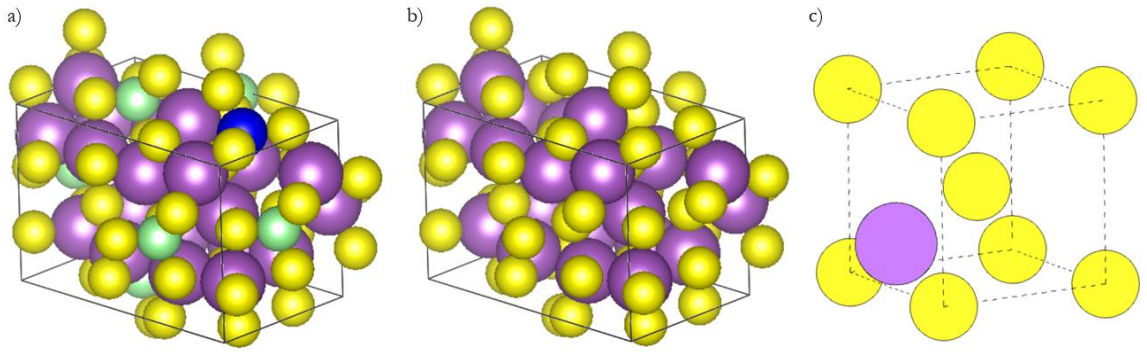

Figure 5. Anion sublattice mapping. a) Existing superionic conductor $Li_{10}GeP_2S_{12}$ (LGPS) [12]. b) LGPS with Ge (blue) and P (green) removed. c) LGPS ultimately maps closely to a single bcc unit cell of sulfur anions with one lithium ion in a tetrahedral site [13]. Sulfur anions in yellow, Li-ions in purple.

1.4 Project Statement & Scope

The goal of this thesis is to replicate the work of Wang *et al.* and to confirm the following salient conclusions from their work: first, that body-centered cubic crystal structures are the most ideal for ionic conduction due to their homogenous tetrahedral interstitial sites and, second, that an anion sublattice is the most important physical characteristic contributing to ionic conductivity and is therefore sufficient for modelling a crystal structure. The purpose of verifying these powerful conclusions is to contribute to a more widespread use of DFT in battery materials research and to subsequently accelerate the progress of battery materials R&D.

Chapter Two – Methods

2.1 Selecting Crystal Structures

The first step for any structural energy investigation is to build the crystal structures in question, which was completed in the Atomic Simulation Environment [13]. To replicate the results of Wang *et al.*, body-centered cubic (BCC), face-centered cubic (FCC), and hexagonal close packing (HCP) crystal structures were constructed for seven different volumes: 28.5, 34, 40, 46.6, 54, 62.1, and 70.8 [$Å^3$] per S atom. Note that Wang *et al.* used volume per S atom because their research focused on Li-ions moving through S anion sublattices. For this thesis, the seven volumes were used for both sulfur anion sublattices as well as oxygen anion sublattices (hence, volume per O atom). These crystal structures and volumes were applied to four different chemistries: lithium ions in a sulfur lattice (Li-S), lithium ions in an oxygen lattice (Li-O), sodium ions in a sulfur lattice (Na-S), and sodium ions in an oxygen lattice (Na-O). In summary, four chemistries, three structures, and seven volumes results in 84 different cases to be investigated.

It is also important to note that these structures are not necessarily based on materials that exist in the real world. As described in Section 1.3 Using Density Functional Theory to Investigate Ionic Conductivity, it is only necessary to perform DFT calculations on the anion sublattice framework within a material to make inferences about that material's ionic conductivity. So, regardless of whether the crystal structures in this study are usable in batteries themselves, the knowledge gained about how particular frameworks affect the ionic conductivity of actual materials will be useful in identifying and designing superionic conductors.

2.2 Interstitial Sites and Ion Hopping Paths

The second step in the DFT energy calculation process is to perform ground-state energy relaxation calculations when the cations are in the anion lattice interstitial sites. The interstitial sites should be stable locations where the energy of the structure is the lowest locally. Since the ions move through solid electrolytes by hopping between interstitial sites, each interstitial site can be thought of as the beginning and endpoints, or the initial and final states, of any migration path. The NEB calculation results are used to plot the change in energy as an ion moves from one interstitial site to the next, so the ground-state energies of the initial and final states are necessary precursors to interpolating the migration path between interstitial sites.

For the BCC structures, there is only one possible path through the unit cell: T1-T2. The T-T movement in BCC structures is illustrated in Figure 6. This means the ion hops directly from tetrahedral site T1 to tetrahedral site T2. For each BCC structure, only one energy landscape will be generated because there is only one possible path for movement.

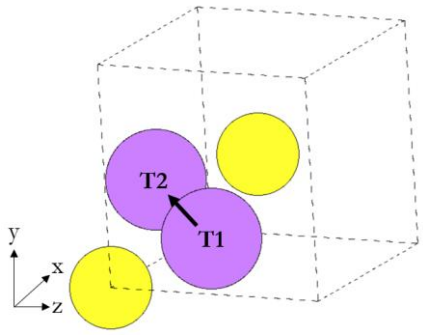

Figure 6. Li-ion migration between tetrahedral sites T1 and T2 in a primitive BCC sulfur cell.

For the FCC structures, there is only one possible path through the unit cell: T1-O1-T2. The T-O-T movement in FCC structures is illustrated in Figure 7. This means the ion must hop from the T1 site to the O1 site before returning to the T2 site. Note that a direct path from the T1 site to the T2 site was not considered as it was assumed that the energy barrier would be too prohibitive for ion diffusion [6]. When moving from the T1 to the O1 position,

only one bond will be broken, but when moving directly from T1 to T2, two bonds must be broken, resulting in a higher activation energy. For each FCC structure, only one energy landscape will be generated because there is only one possible path for movement.

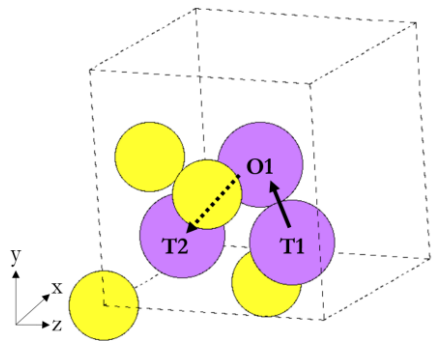

Figure 7. Li-ion migration from tetrahedral site T1 to octahedral site O1 and finally to tetrahedral site T2 in a primitive FCC sulfur cell.

For HCP structures, there are three possible paths through the unit cell: T1-O1-T2, T1-T3, and O1-O2. All migration paths within an HCP structure are illustrated in Figure 8. As in BCC and FCC structures, ions can move in a T-O-T path or a T-T path, but they can also move from one octahedral site to another in an O-O path. For each HCP structure, three energy landscapes will be generated because there are three possible paths for movement.

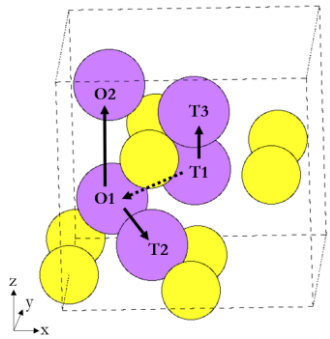

Figure 8. Li-ion migration in a primitive HCP sulfur cell. There are three paths for ionic interstitial hopping: tetrahedral to tetrahedral (T1-T3), tetrahedral to octahedral to tetrahedral (T1-O1-T2), and octahedral to octahedral (O1-O2).

To summarize, for the four different chemistries, seven volumes were considered. For those seven volumes, three different crystal structures were investigated. And for those three structures, the energy landscape for each possible path (T-T, O-O, T-O-T) were calculated.

2.3 DFT Workflow

The workflow for performing DFT calculations begins with using the Atomic Simulation Environment to generate the crystal structures. Because the DFT calculations were performed using the Vienna Ab Initio Simulation Package (VASP), the crystal structures were written to a VASP file called a POSCAR.

The VASP pseudopotentials that contain all the information about each element in the crystal structure are saved in the POTCAR file. Depending on the case being calculated, this file contains information on either Li and S, Li and O, Na and S, or Na and O. For this thesis, these POTCARs have been altered to reflect the ions for each element rather than the atom. For example, the POTCAR would normally read that sulfur has 6 valence electrons and Li has 1, but for these calculations, it has been modified to show that sulfur has 8 valence electrons (to make S^{2-}) and Li has 0 (to make Li^{+}).

All the desired calculation settings and parameters are written to a VASP file called the INCAR; the specific parameters used can be found in the Appendix. It is highly relevant to note that in order to perform calculations on an anion lattice, it is necessary to use the INCAR file to add a uniform background charge to the cell. VASP requires a neutral system, which is not useful for modelling solid-state electrolytes because the application of an electrolyte in a battery in and of itself implies that the ions must be charged. To achieve an accurate charge that is still compatible with VASP's operation requirements, a uniform background charge is assumed. For example, in the Li-S BCC case, the realistic, charged model would have 16 valence electrons (8 per S^{2-}, 0 per Li^{+}), and the neutral model would have 13 valence electrons

(6 per S, 1 per Li). In order to balance the system, the NELECT tag is set to 13 in the INCAR file, so VASP will subtract 13 from 16 to add 3 positive background charges to the calculation. Figure 9 provides a visual representation for how the uniform background charge is implemented.

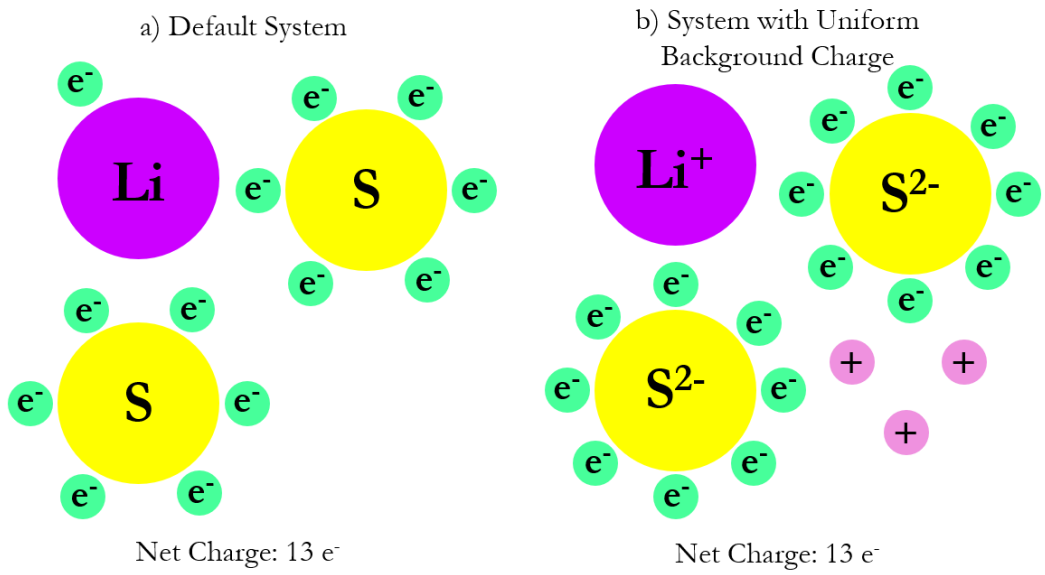

Figure 9. Illustration of how VASP incorporates a uniform background charge.

To put it broadly, DFT relaxation calculations rely on an iterative process of using the electronic density of a crystal structure to calculate the energy of the configuration, checking if the forces in the system are low enough to be considered converged, and then either exiting or repeating the process (refer to Figure 3). During this study, it was discovered that in order for VASP to make correct initial guesses for the atom positions when the uniform background charge was in use (henceforth to be referred to as the "charged system"), VASP was inexplicably unable to generate an initial guess for the atom positions. Thus, it was determined that a WAVECAR, a VASP file containing information on the atom positions, must be supplied as an input to the calculation. The WAVECAR was generated by first performing a ground-state energy calculation on a neutral system (no altered POTCARs and no uniform

background charge) to determine initial atom positions, and then, this WAVECAR was used in all charged system DFT calculations.

2.4 Nudged Elastic Band Calculations

Once the ground-state energies for the initial and final states had been calculated, NEB theory was applied to find the energy landscapes for an ion migration path. First, a physical path between the initial and final states was approximated, as shown in Figure 10.

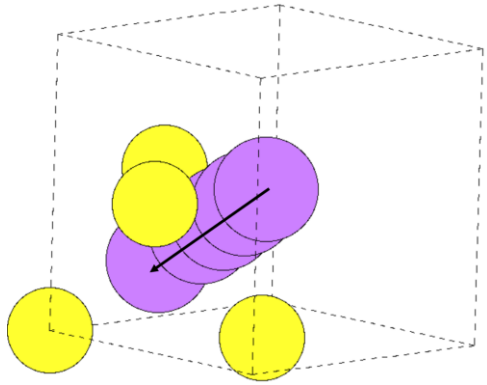

Figure 10. Example of how an Li-ion migration path is interpolated for an NEB calculation.

Second, as with the ground-state calculations, the WAVECAR files from the initial and final state calculations are copied into the NEB folders. This is necessary so that VASP can set reasonable starting positions for the NEB.

Third, the NEB calculations are run. The calculations finally finished when the forces were lower than the EDIFFG value, a tag in the INCAR file that denotes the exit condition for the ionic relaxation loop; it was frequently necessary to rerun the calculations many times for the NEBs to fully converge.

Chapter Three – Results & Discussion

3.1 Lithium Cations in a Sulfide Framework (Li-S)

3.1.1 Li-S Body-Centered Cubic

Figure 11 shows the energy landscapes of a lithium ion in a BCC sulfur anion sublattice. The general parabolic shape of these curves is intuitive (and consistent with the shape of the energy landscapes produced by Wang *et al.*, shown in Figure 12): the energies are the lowest at the tetrahedral sites, and the energy is the highest at the midpoint between the tetrahedral sites where the interatomic forces are the strongest (refer to Figure 6).

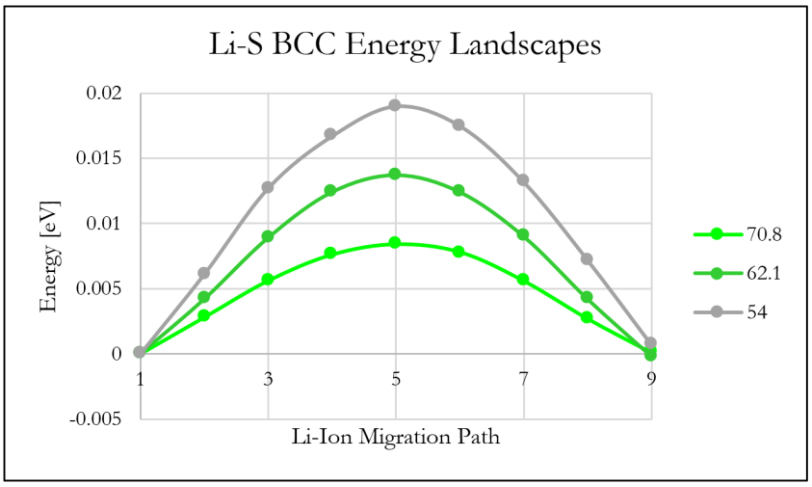

Figure 11. Energy landscapes for a Li-ion migrating through a BCC S anion sublattice via a T-T path.

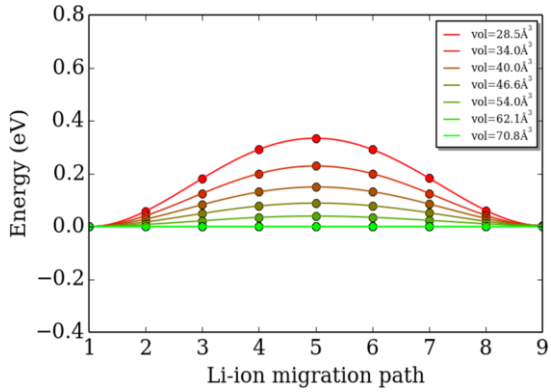

Figure 12. Findings from Wang *et al.* of the energy landscapes for a Li-ion migrating through a BCC S anion sublattice via a T-T path [6].

3.1.2 Li-S Face Centered Cubic

Figure 13 shows the energy landscapes of a lithium ion in an FCC sulfur anion sublattice. The shapes of the energy landscapes are reasonable considering the path the ion must take in an FCC structure (refer to Figure 7). The ion begins at a tetrahedral site and overcomes a small energy barrier to move to an octahedral site, where it settles. Then, from the octahedral site, the ion must overcome another energy barrier to move to its final tetrahedral site.

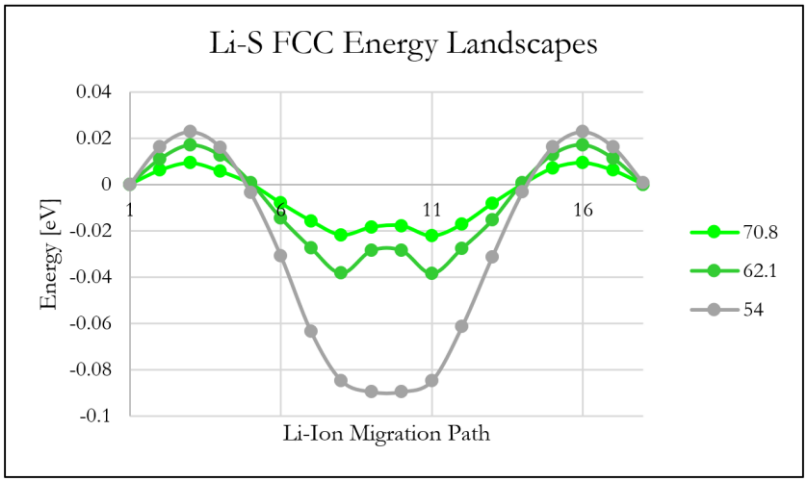

Figure 13. Energy landscapes for a Li-ion migrating through an FCC S anion sublattice via a T-O-T path.

While the shapes of the curves in Figure 13 seem reasonable, there is a slight inconsistency between these results and those produced by Wang *et al.*, seen in Figure 14. Wang *et al.*'s results show that all energy landscapes for calculations that used a unit cell volume of ≥46.6 [$Å^3$] per S should be concave-down with the highest energy barrier at the central octahedral site. The

curves in Figure 13, which all correspond to structures with volumes above 46.6 [Å^3] per S, seem to exhibit the energy landscapes for less voluminous cells.

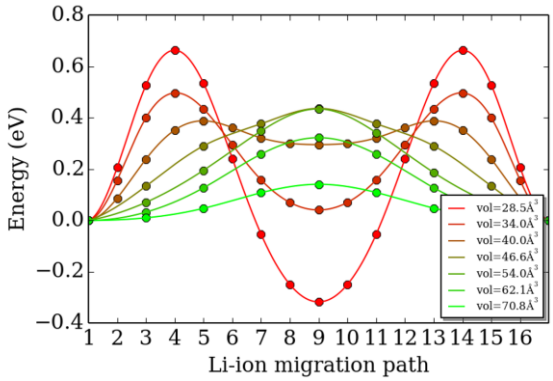

Figure 14. Findings from Wang *et al.* of the energy landscapes for a Li-ion migrating through an FCC S anion sublattice via a T-O-T path [6].

3.1.3 Li-S Hexagonal Close Packing

Figure 15 shows the energy landscapes of a lithium ion in an HCP sulfur anion sublattice via the T-T migration path. The ion begins at a tetrahedral site and overcomes an energy barrier to move to its final tetrahedral site. It was expected that the initial and final state energies would be the same with a maximum energy barrier at the midpoint between the tetrahedral sites, as in the results from Wang *et al.* shown in Figure 16.

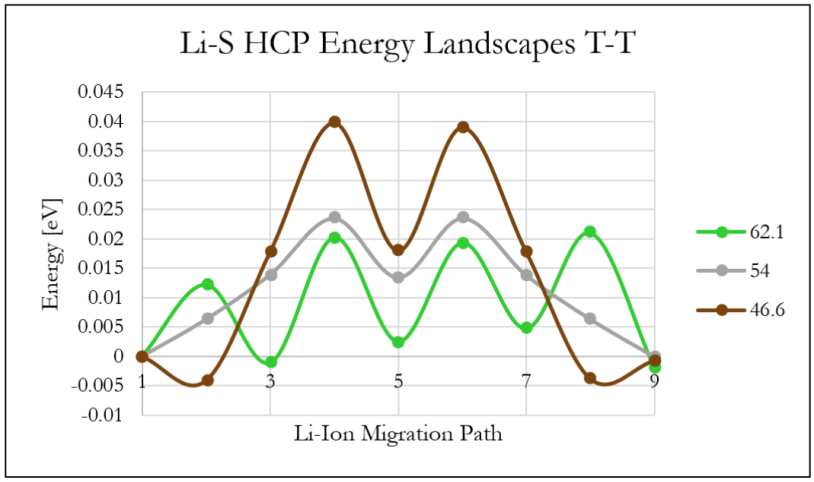

Figure 15. Energy landscapes for a Li-ion migrating through an HCP S anion sublattice via a T-T path.

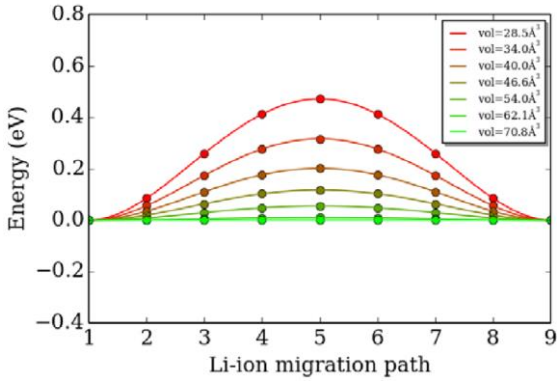

Figure 16. Findings from Wang *et al.* of the energy landscapes for a Li-ion migrating through an HCP S anion sublattice via a T-T path [6].

Figure 17 shows the energy landscapes of a lithium ion in an HCP sulfur anion sublattice via the O-O migration path. The ion begins at an octahedral site and overcomes an energy barrier to move to its final octahedral site. The energy landscapes reflect the expected energetics and are similar to the results from Wang *et al.* shown in Figure 18.

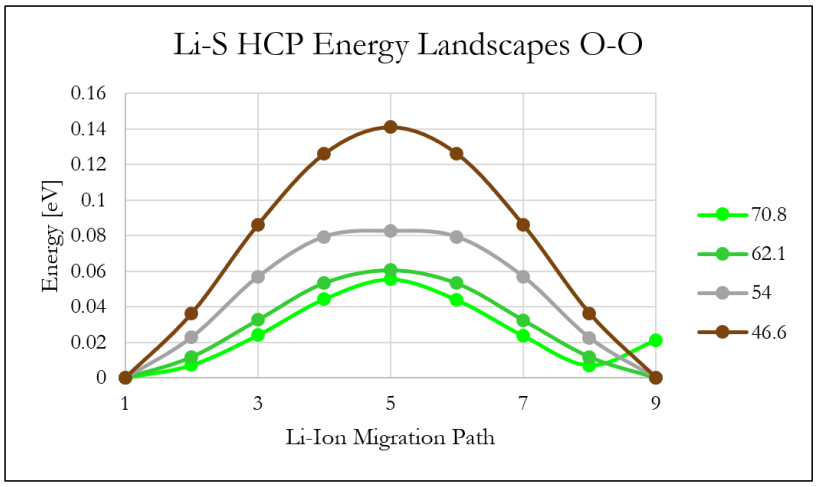

Figure 17. Energy landscapes for a Li-ion migrating through an HCP S anion sublattice via an O-O path.

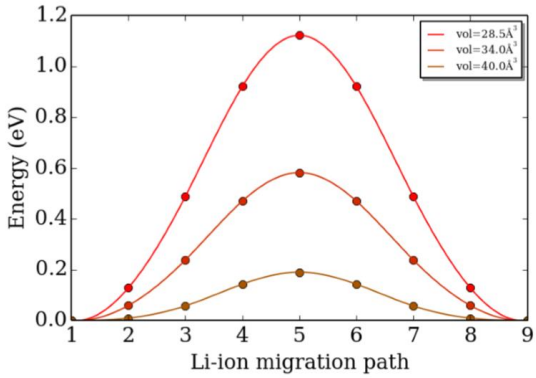

Figure 18. Findings from Wang *et al.* of the energy landscapes for a Li-ion migrating through an HCP S anion sublattice via an O-O path [6].

Figure 19 shows the energy landscapes of a lithium ion in an HCP sulfur anion sublattice via the T-O-T migration path. Like the FCC structures, the Li-ion begins at a tetrahedral site and overcomes an energy barrier to move to an octahedral site, where it settles, and from the octahedral site, the ion must overcome another energy barrier to move to its final tetrahedral site.

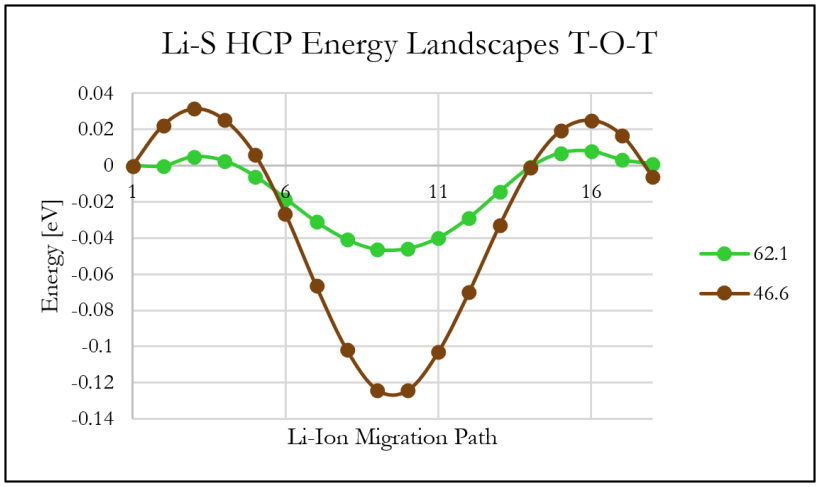

Figure 19. Energy landscapes for a Li-ion migrating through an HCP S anion sublattice via a T-O-T path.

Figure 20 shows the energy landscapes produced by Wang *et al.* for a Li-ion migrating through an HCP sulfur anion sublattice following at T-O-T path.

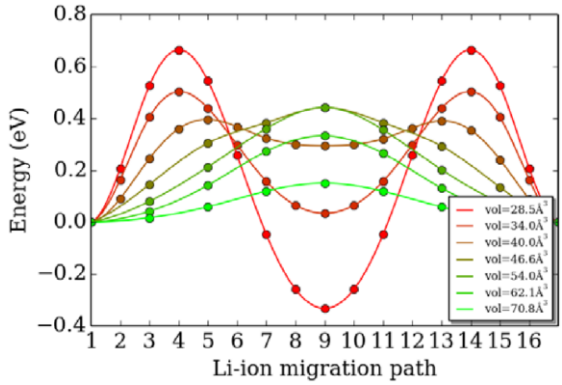

Figure 20. Findings from Wang *et al.* of the energy landscapes for a Li-ion migrating through an HCP S anion sublattice via a T-O-T path [6].

3.1.4 Activation Energy for Li-ion Migration in S Anion Framework vs. Volume

Identifying trends between energy and cell volume is also important as there is, or should be, a range of volumes for which the energy of a crystal structure is optimized. Typically, it is expected that larger cell volumes will have the lowest energy barriers. When the atoms in a structure are relatively far apart, their interatomic forces are weaker, and thus, less energy is required to overcome said forces.

Figure 21 shows the correlation between activation energy and unit cell volume for Li-S structures. These curves are consistent with the hypothesis that larger volumes have lower activation energies due to lower interatomic forces; this is consistent for all crystal structures (BCC, FCC, & HCP) and for all energy pathways (T-T, O-O, & T-O-T). In addition, FCC structures are also shown to have higher activation energies than BCC structures across all volumes. FCC unit cells contain more atoms than BCC cells, which increases that amount of interatomic force that a Li-ion would experience while migrating through the structure.

Therefore, it is understandable that FCC structures would have higher activation energies than BCC structures overall.

Interestingly, the TT path in HCP structure has comparable energy-volume relationships to the BCC structures. This shows that direct movement between tetrahedral sites of equivalent energy is ideal for ion diffusion, regardless of whether the anion sublattice is a BCC or HCP structure.

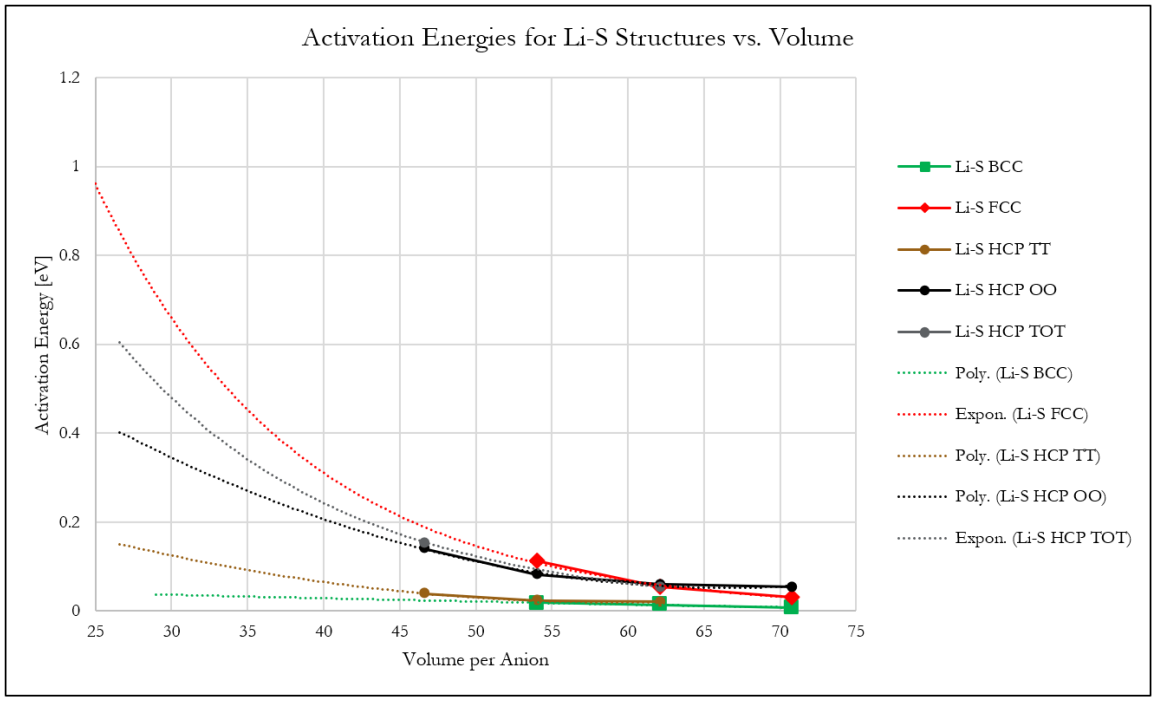

Figure 21. Energy barriers versus cell volume per S anion for various Li-S crystal structures. The dotted lines show the expected trends.

For comparison, Figure 22 shows the plots for energy barriers (activation energy) versus cell volume for Li-S structures generated by Wang *et al.* Their plots show the same three phenomena: first, FCC structures have higher activation energies for all volumes; second, activation energies are generally lower for higher volumes; and third, ion migration paths that move directly between interstitial sites of equivalent energies (T-T or O-O) typically have the lowest energy barriers.

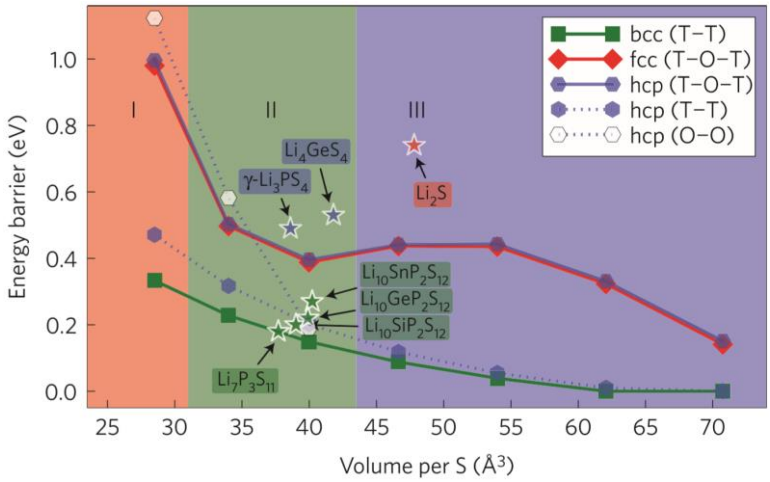

Figure 22. Findings from previous work of the energy barriers versus cell volume per S anion for various Li-S crystal structures [6].

3.2 Sodium Cations in a Sulfide Framework (Na-S)

3.2.1 Na-S Body-Centered Cubic

Like the Li-S BCC energy landscapes, the energy landscapes for sodium ions migrating through a sulfur anion sublattice, seen in Figure 23, are parabolic-shaped. The similarities between the Li-S and Na-S BCC energy landscapes serve as evidence that elements within the same group on the periodic table (and thus with the same number of valence electrons) exhibit similar ion diffusion characteristics. Though, it should also be noted that the activation energies of the Li-S BCC cases were lower than those in the Na-S BCC cases; this is likely due to the relative atomic masses (6.94 [u] for Li and 22.99 [u] for Na) and radii (182 [pm] for Li

and 227 [pm] for Na) of lithium and sodium. Lithium, being lighter and less voluminous, requires less energy to move between tetrahedral sites in a sulfur framework.

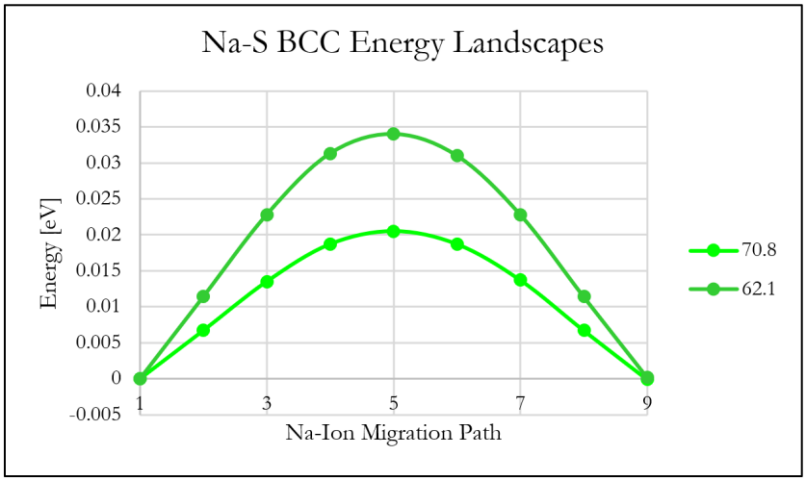

Figure 23. Energy landscapes for a Na-ion migrating through a BCC S anion sublattice via a T-T path.

3.2.2 Na-S Face-Centered Cubic

Figure 24 shows the energy pathway of a sodium ion in an FCC sulfur anion sublattice.

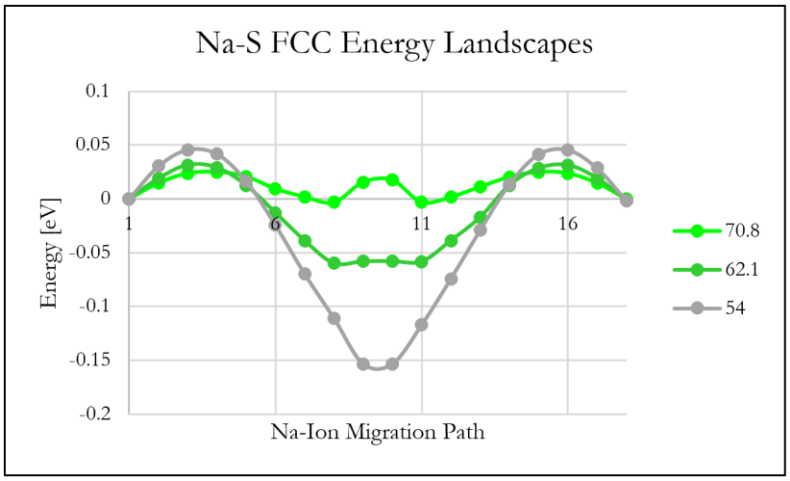

Figure 24. Energy landscapes for a Na-ion migrating through an FCC S anion sublattice via a T-O-T path.

The energy landscapes of sodium ions migrating through a sulfur anion sublattice, seen in Figure 24, have a similar shape to the Li-S FCC landscapes in Figure 13. The energies are at local minima at the tetrahedral and octahedral sites and reach local maxima when moving from T1 to O1 or O2 to T2. As with the BCC cases, the similarities between the Li-S and Na-S FCC

cases suggest that positive charge carriers from the same period table group diffuse through crystal structures in the same way.

3.2.3 Na-S Hexagonal Close Packing

Figure 25 shows the energy landscapes of a sodium ion migrating through an HCP sulfur anion sublattice via the T-T migration path. The ion begins at a tetrahedral site and overcomes an energy barrier to move to its final tetrahedral site, so it was expected that the initial and final state energies would be the same with a maximum energy barrier at the midpoint between the tetrahedral sites. This expectation was confirmed in the energy landscapes for the 54 and 62.1[Å^3] per S cases.

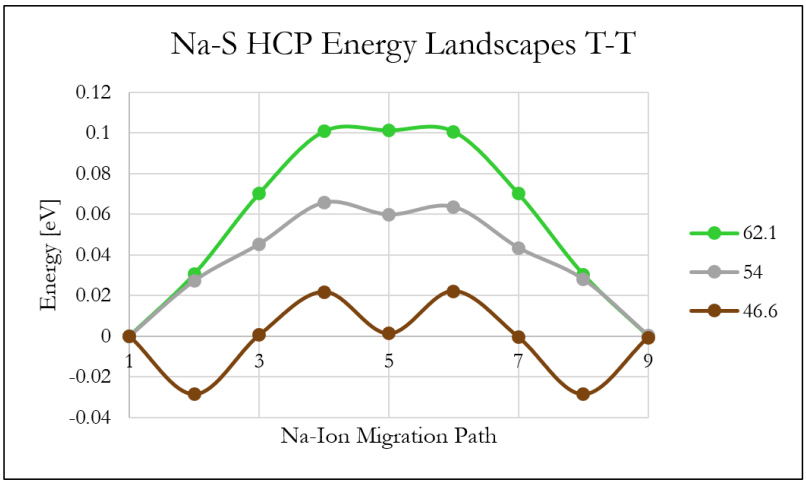

Figure 25. Energy landscapes for a Na-ion migrating through an HCP S anion sublattice via a T-T path.

Figure 26 shows the energy landscapes of a sodium ion migrating through an HCP sulfur anion sublattice via the O-O migration path. Like the T-T pathway, it was expected that the initial and final state energies would be the same with a maximum energy barrier at the midpoint between the octahedral sites, and also like the T-T results in Figure 25, the 54 and 62.1 [Å^3] per S cases exhibit the expected behavior.

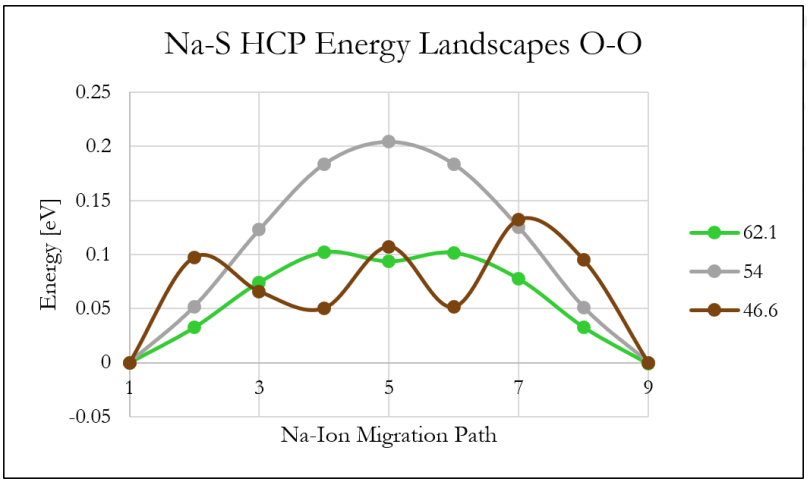

Figure 26. Energy landscapes for a Na-ion migrating through an HCP S anion sublattice via an O-O path.

Figure 27 shows the energy pathway of a sodium ion migrating through an HCP sulfur anion sublattice via the T-O-T migration path.

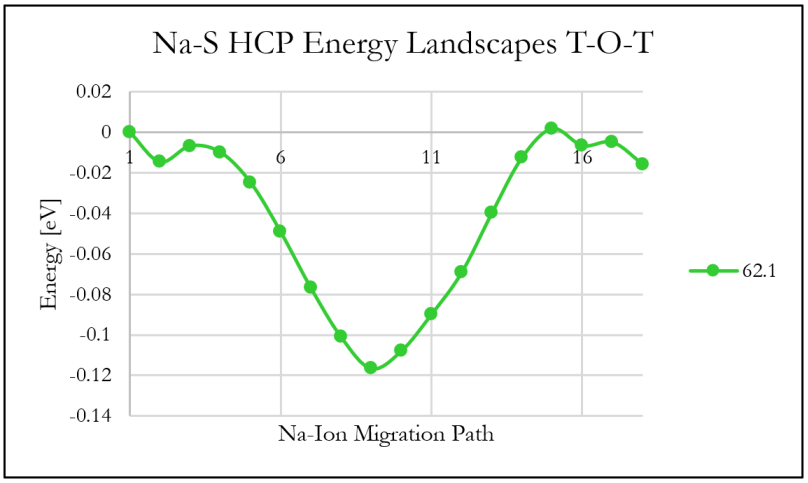

Figure 27. Energy landscapes for a Na-ion migrating through an HCP S anion sublattice via a T-O-T path.

3.2.4 Activation Energy for Na-ion Migration in S Anion Framework vs. Volume

Figure 28 shows the correlation between activation energy and unit cell volume for the Na-S cases. The results of Figure 28 remain consistent with previous conclusions: BCC structures have lower activation energy barriers than FCC structures, and activation energies

decrease as cell volume increases. For comparison, Figure 29 shows the plots for activation energy versus cell volume for Na-S structures generated by Wang *et al.*

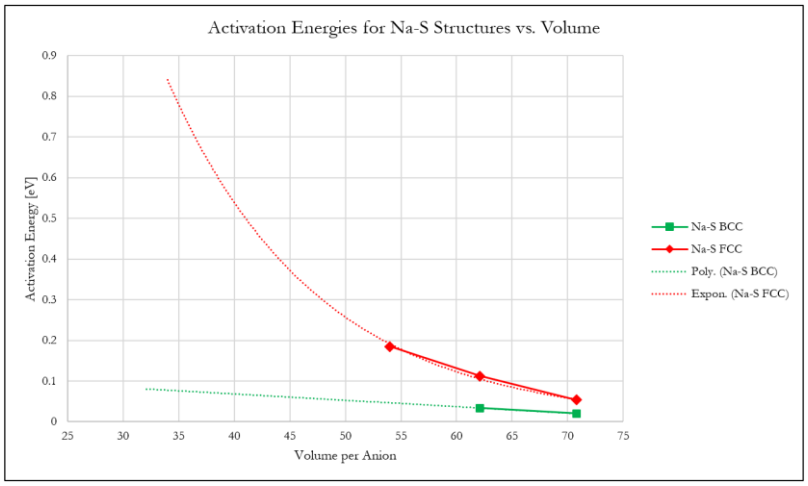

Figure 28. Energy barriers versus cell volume per S anion for various Na-S crystal structures.

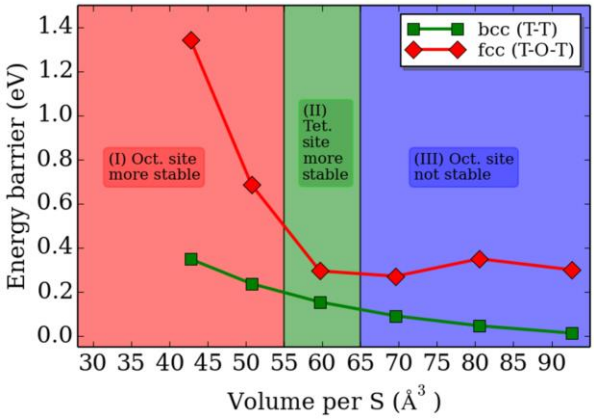

Figure 29. Findings from Wang *et al.* of the energy barriers versus cell volume per S anion for various Na-S crystal structures [6].

3.3 Lithium Cations in an Oxide Framework (Li-O)

3.3.1 Li-O Body-Centered Cubic

Figure 30 shows the energy landscapes of a lithium ion through a BCC oxygen anion sublattice. While the curves may seem to differ greatly from the clean parabolic shapes from the BCC sulfide cases, the differences are in the range of 10^{-3} [eV], which is most likely within the accuracy of the calculation. In general, the energy landscapes begin and end around 0 [eV].

For the large volumes (≥46.6 [Å^3] per O), disregarding the outlying data point in the 70.8 [Å^3] per O curve, the energy landscapes are relatively flat, suggesting that Li-O BCC structures might make for a promising superionic conductor.

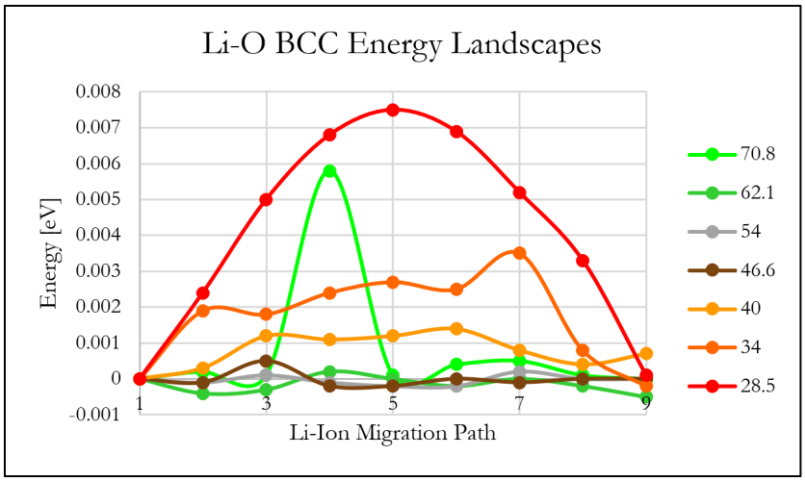

Figure 30. Energy landscapes for a Li-ion migrating through a BCC O anion sublattice via a T-T path.

3.3.2 Li-O Face-Centered Cubic

Figure 31 shows the energy landscapes of a lithium ion in an FCC oxygen anion sublattice.

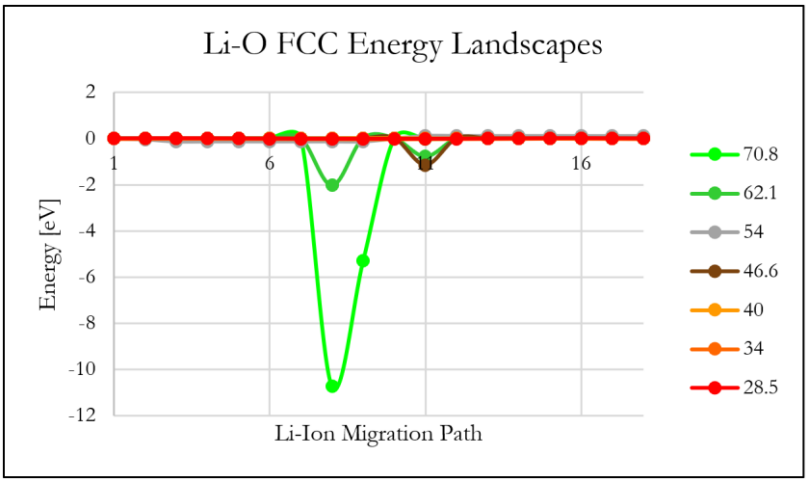

Figure 31. Energy landscapes for a Li-ion migrating through an FCC O anion sublattice via a T-O-T path.

3.3.3 Li-O Hexagonal Close Packing

Figure 32 shows the energy landscapes of a lithium ion in an HCP oxygen anion sublattice via the T-T migration path.

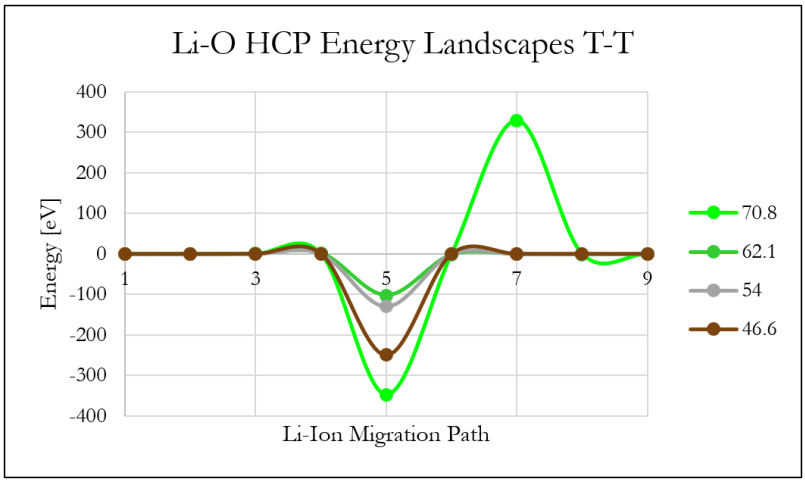

Figure 32. Energy landscapes for a Li-ion migrating through an HCP O anion sublattice via a T-T path.

Figure 33 and Figure 34 show the energy pathways of a lithium ion in an HCP oxygen anion sublattice via the O-O and T-O-T migration paths, respectively.

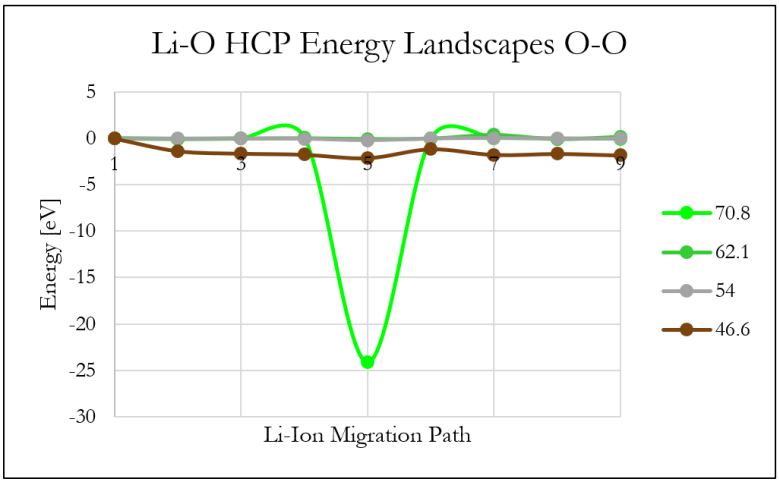

Figure 33. Energy landscapes for a Li-ion migrating through an HCP O anion sublattice via an O-O path.

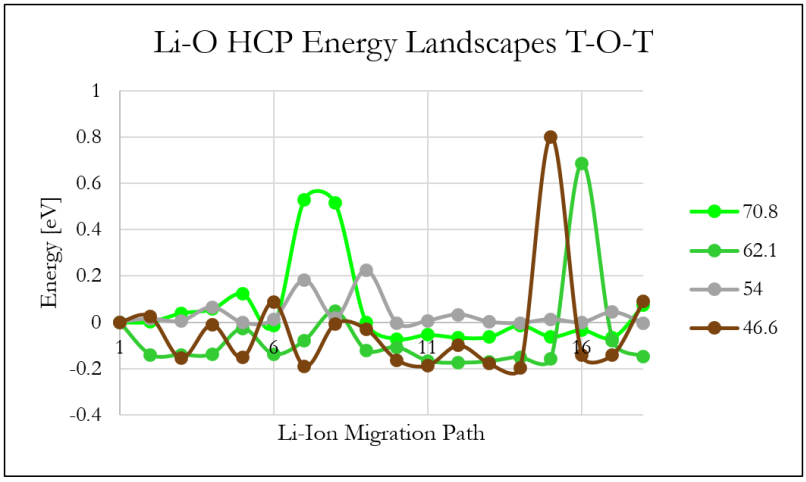

Figure 34. Energy landscapes for a Li-ion migrating through an HCP O anion sublattice via a T-O-T path.

3.3.4 Activation Energy for Li-ion Migration in O Anion Framework vs. Volume

Figure 35 shows the correlation between activation energy and unit cell volume for the Li-O cases. The Li-O FCC and HCP energy vs. volume results are excluded given that the energy landscapes on which they are based are unrealistic. Regardless, the relationship between activation energy and volume is realistic for the Li-O BCC cases and has a similar curvature to Wang *et al.*'s findings, shown in Figure 36.

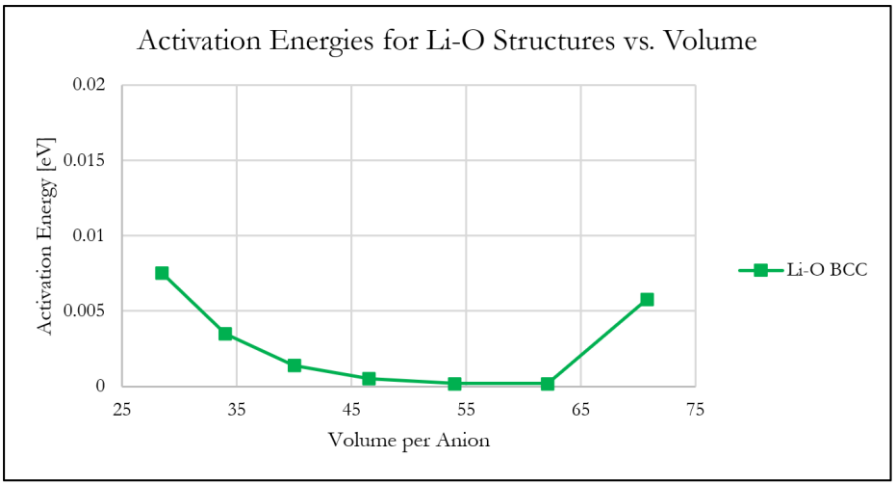

Figure 35. Energy barriers versus cell volume per O anion for various Li-O crystal structures.

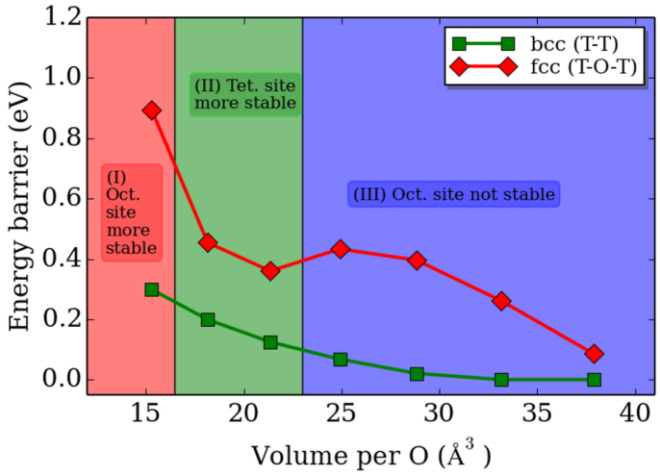

Figure 36. Findings from Wang *et al.* of the energy barriers versus cell volume per O anion for various Li-O crystal structures [6].

3.4 Sodium Cations in an Oxide Framework (Na-O)

3.4.1 Na-O Body-Centered Cubic

Figure 37 shows the energy pathways of a sodium ion in a BCC oxygen anion sublattice. These curves are intuitive in that they all have a general parabolic shape, begin and end at 0 [eV], and have increasing maxima as cell volume decreases. However, it is surprising that the intermediate position was found to have a lower energy than the endpoint tetrahedral sites for the 54, 62.1, and 70.8 [Å^3] per O cases. Though, as mentioned for the Li-O cases, the order of the energies suggests that this deviation is likely within the accuracy of the calculations. The similarity of the Na-O BCC landscapes to both the Li-S and Na-S BCC landscapes support

the idea that anion lattices consisting of elements from the same periodic groups have similar structural energies.

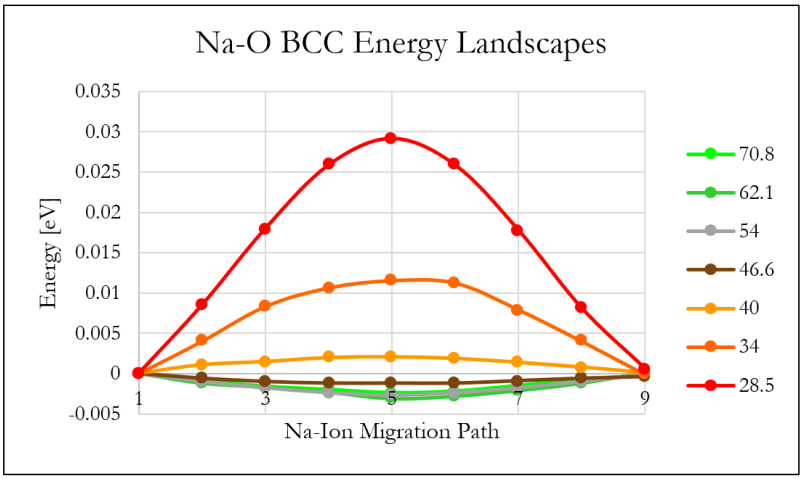

Figure 37. Energy landscapes for a Na-ion migrating through a BCC O anion sublattice via a T-T path.

3.4.2 Na-O Face-Centered Cubic

Figure 38 shows the energy landscapes of a sodium ion in an FCC oxygen anion sublattice.

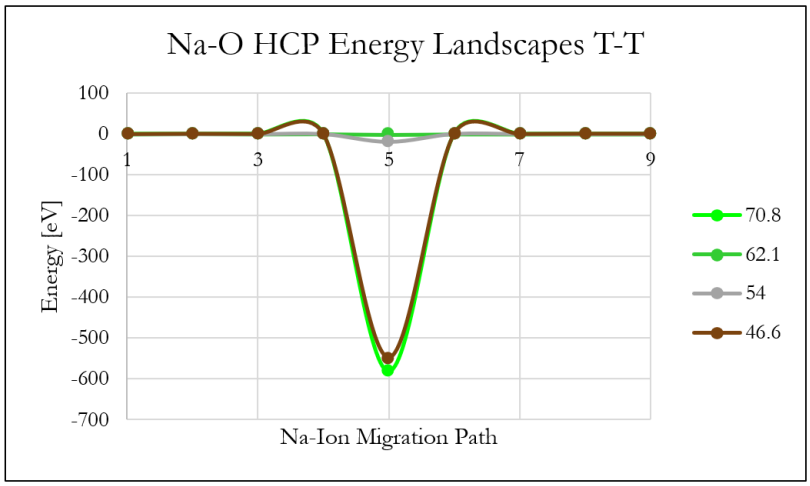

Figure 38. Energy landscapes for a Na-ion migrating through an FCC O anion sublattice via a T-O-T path.

Figure 39, Figure 40, and Figure 41show the energy pathways of a sodium ion in an HCP oxygen anion sublattice via the T-T, O-O, and T-O-T pathways, respectively.

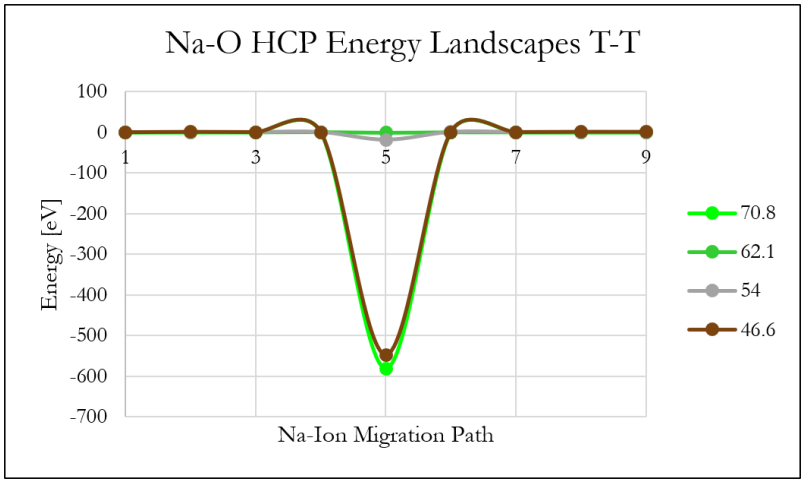

Figure 39. Energy landscapes for a Na-ion migrating through an HCP O anion sublattice via a T-T path.

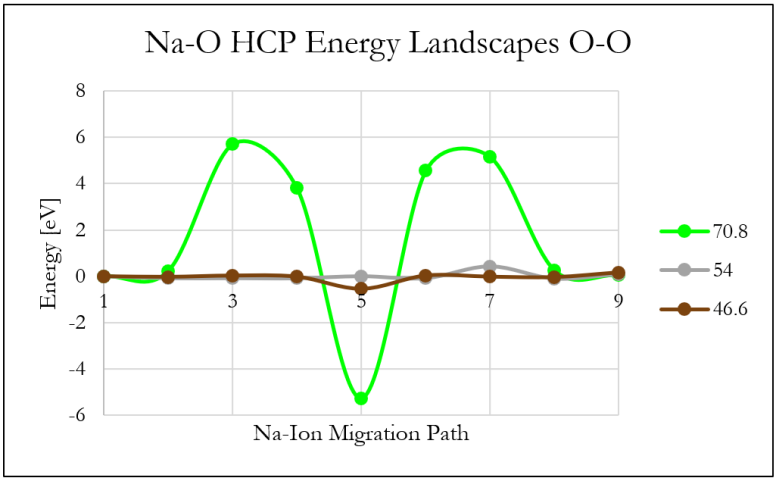

Figure 40. Energy landscapes for a Na-ion migrating through an HCP O anion sublattice via an O-O path.

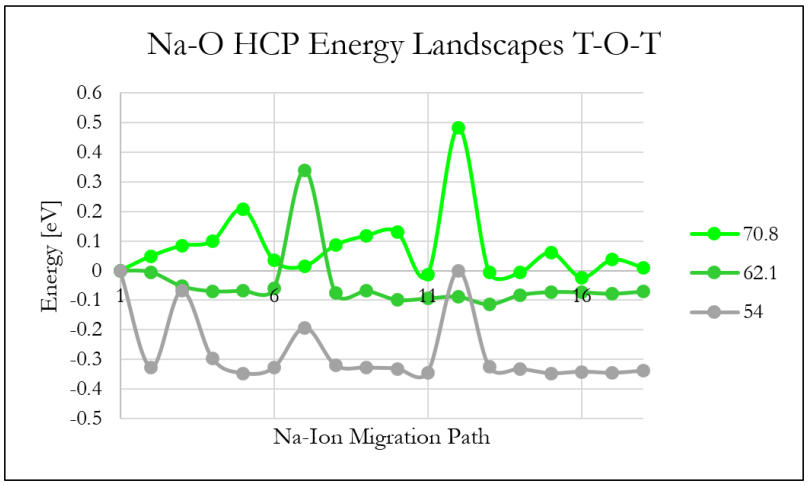

Figure 41. Energy landscapes for a Na-ion migrating through an HCP O anion sublattice via a T-O-T path.

3.4.4 Activation Energy for Na-ion Migration in O Anion Framework vs. Volume

Figure 42 shows the correlation between activation energy and unit cell volume for the Na-O cases. The Na-O FCC and HCP curves were excluded as those energy landscapes are unrealistic. The Na-O BCC energy vs. volume curve is as expected with activation energy decreasing as volume increases.

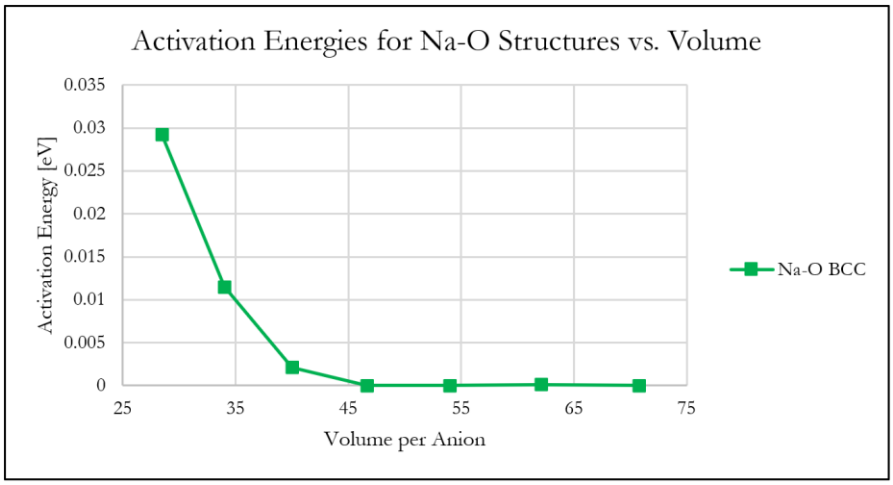

Figure 42. Energy barriers versus cell volume per O anion for various Na-O crystal structures.

3.5 Limitations of Current Results

While many of the results in this thesis follow expected trends, there are a few cases that have produced surprising and unrealistic data. For those perplexing cases, the following inferences have been made regarding their causes and possible remedies.

First, for all the energy landscapes, there is a notable difference in the range of the energies seen on the y-axis from what is expected. The energies in this thesis are approximately an order of 10 times smaller than those produced by Wang *et al.* This is likely the result of a difference in DFT calculation techniques. In particular, the results for this thesis were generated by performing calculations on singular primitive unit cells, while Wang *et al.* used 3x3x3 supercells, which are the same unit cells multiplied three times in each direction. Using only a single unit cell may have distorted the forces, and thus the energies of the crystal

structures, whereas a 3x3x3 supercell is better representative of the interatomic forces that would be present throughout a real material.

Second, the FCC and HCP oxide cases showed energy landscapes that were counterintuitive. The results presented did not take into account the electron spin of the oxygen valence electrons, but it is thought that this many have an effect on the energies. For example, the occupation of the orbitals for oxygen atoms determines the bandgap energies. If these bandgap energies are too large (which was the case for the generated results), then the electron density that VASP assumes will likely be incorrect, ultimately resulting in an incorrect final energy calculation.

Third, the smearing function, which determines the electron distribution used by VASP, shall be changed. As shown in the Appendix, an ISMEAR value was not set in the INCARs. It is believed that changing the smearing function to the Tetrahedron method with Blöchl corrections (ISMEAR = -5) will improve the results as this is the preferred setting for insulators.

Chapter Four – Summary and Conclusions

In conclusion, density functional theory coupled with nudged elastic band theory was used to study the structural energies of solid-state electrolytes. Density functional theory calculations were performed for body-centered cubic, face-centered cubic, and hexagonal close packing structures for four chemistries (Li-S, Na-S, Li-O, Li-O) over a range of seven volumes. Combing DFT with nudge elastic band theory produced energy landscapes, which showed the energy necessary for a cation to hop between interstitial sites for each of the chemistry/structure/volume cases. The energy landscapes revealed three major conclusions:

First, the activation energies for ions migrating through BCC structures were consistently lower than ions migrating through FCC and HCP structures across all chemistries and volumes, though the HCP structures for the T-T and O-O cases were quite comparable. This finding shows that BCC anion sublattices are ideal for Li-ion transport due to their homogenous tetrahedral sites. Therefore, materials with crystallographically equivalent substructures should be favored by designers, but if this is not achievable, a heterogenous structure in which a mobile cation has the possibility of hopping via T-T and/or O-O paths would be the next best option.

Second, energy barriers tend to decrease as unit cell volume increases. This suggests that, in general, a larger unit cell volume is desirable as it lowers the energy required for a migrating cation to overcome the interatomic forces. Materials designers will need to find a balance between optimizing unit cell volume for ion diffusion purposes and maintaining a practical battery size.

Third, the energy landscapes for all four chemistries were similar. This suggests that elements in the same groups on the period table (and thus with the same number of valence electrons) have either similar transport mechanisms (Li and Na) or structural properties (S and O). However, this study only accounted for cations in the alkali metal group and anions in the chalcogen group, so it is possible that crystal structures with components from other groups could have similar structural energies. Regardless, the hypothesis that Li- and Na-ions could diffuse through S and O lattices in similar ways was proved to be true. More investigation is necessary to definitively say whether transport properties are affected by the valency of the structural components.

The breadth of this project could be expanded in a variety of ways. Investigating more chemistries is an obvious route; two elements of particular interest are Mg^{2+} and Se^{2-}. Mg^{2+} is

interesting because having a charge carrier that supplies 2 valence electrons would double the charge that could be extracted from a typical Li-ion battery. However, designing a Mg-ion electrolyte is especially challenging due to the size of the Mg-ion. In addition, Se^{2-} is also worth investigating because according to a study by Canepa *et al.*, Se^{2-} anion sublattices have even lower energy barriers than oxides or sulfides and may be especially applicable for Mg-ion diffusion [14].

The purpose of this thesis was to be a proof-of-concept for using *ab initio* simulations for solid-state electrolyte design. Although batteries are one of the most necessary and important technologies for energy sustainability, the rate at which they are developed and improved lags far behind what is currently needed. For batteries, adhering to Moore's Law, that is to say doubling performance metrics every 18 months, is likely an unattainable goal, but significant accelerations in progress can be made by implementing high performance computing more frequently in battery materials research. This thesis shows that density functional theory calculations can provide reasonable and repeatable results, though there can be inconsistencies due to calculation settings, inaccurate modeling, etc. Therefore, it is recommended that future solid-state electrolyte research utilize DFT as a precursor to all experimental research, serving as a filter that determines where physical resources and time shall be allocated in the experimental phase.

References

[1] A. Z. Weber, M. M. Mench, J. P. Meyers, P. N. Ross, J. T. Gostick and Q. Liu, "Redox flow batteries: a review," *Journal of Applied Electrochemistry,* pp. 1137-1164, 2011.

[2] Y. Yao, *Lecture 6: Introduction to Li-ion Batteries and Negative Electrodes,* Houston, 2019.

[3] Y. Liang, Y. Jing, S. Gheytani, K.-Y. Lee, P. Liu, A. Facchetti and Y. Yao, "Universal quinone electrodes for long cycle life aqueous rechargable batteries," *Nature Materials,* vol. 16, pp. 841-848, 2017.

[4] R. A. Huggins, Advanced Batteries: Materials Science Aspects, Stanford, California: Springer Science+Business Media, 2009.

[5] J. Liu, "Addressing the Grand Challenges in Energy Storage," *Advanced Functional Materials,* vol. 23, no. 8, pp. 924-928, 2013.

[6] Y. Wang, W. D. Richards, S. P. Ong, L. J. Miara, J. C. Kim, Y. Mo and G. Ceder, "Design principles for solid-state lithium superionic conductors," *Nature Materials,* pp. 1026 - 1032, 2015.

[7] A. Manthiram, X. Yu and S. Wang, "Lithium battery chemistries enabled by solid-state electrolyes," *Nature Reviews Materials,* vol. 2, no. Article Number 16103, pp. 1-16, 2017.

[8] P. Canepa, S.-H. Bo, G. S. Gautam, B. Key, W. D. Richards, T. Shi, Y. Tian, Y. Wang, J. Li and G. Ceder, "High magnesium mobility in ternary spinal chalcogenides," *Nature Communications,* pp. 1-8, 2017.

[9] Z. Zhang, E. Ramos, F. Lalère, A. Assoud, K. Kaup, P. Hartman and L. F. Nazar, "Na11Sn2PS12: a new solid state sodium superionic conductor," *Energy & Environmental Science,* pp. 87 - 93, 2017.

[10] R. E. Ciez and J. F. Whitacre, "The cost of lithium is unlikely to upend the price of Li-ion storage systems," *Elsevier Journal of Power Sources,* vol. 320, pp. 310-313, 2016.

[11] D. S. Scholl and J. A. Steckel, Density Functional Theory: A Practical Introduction, Hoboken, New Jersey: John Wiley & Sons, Inc., 2009.

[12] K. Momma and F. Izumi, "VESTA 3 for three-dimensional visualization of crystal, volumetric and morphology data," *Journal of Applied Crystallography,* vol. 4, no. Part 6, pp. 1272-1276, 2011.

[13] A. H. Larsen, J. J. Mortensen, J. Blomqvist, I. E. Castelli, R. Christensen, M. Dułak, J. Friis, M. N. Groves, B. Hammer, C. Hargus, E. D. Hermes, P. C. Jennings, P. B. Jensen, J. Kermode, J. R. Kitchin, E. L. Kolsbjerg, J. Kubal, K. Kaasbjerg, S. Lysgaard, J. B. Maronsson, T. Maxson, T. Olsen, L. Pastewka, A. Peterson, C. Rostgaard, J. Schiøtz, O. Schütt, M. Strange, K. S. Thygesen, T. Vegge, L. Vilhelmsen, M. Walter, Z. Zeng and K. W. Jacobsen, "The Atomic Simulation Environment--A Python Library for working with atoms," *Journal of Physics: Condensed Matter,* vol. 29, p. 273002, 2017.

[14] P. Canepa, S.-H. Bo, S. G. Gautam, B. Key, D. W. Richards, T. Shi, Y. Wang, J. Li and G. Ceder, "High magnesium mobility in ternary spinel chalcogenides," *Nature Communications,* vol. 8, no. 1, p. 1759, 2017.

[15] C. Morris, "Toyota researchers develop all-solid-state Li-ion batteries," Charged Electric Vehicles Magazine, 17 June 2014. [Online]. Available: https://chargedevs.com/newswire/toyota-researchers-develop-all-solid-state-li-ion-batteries/. [Accessed 1 February 2019].

Appendix

DFT Python script for an uncharged Li-S BCC system with Li in the T1 position

```
from ase.io import write
from ase.build import bulk
from ase import Atom
from ase.calculators.vasp import Vasp
import os

os.system('cp ../volume .')
f = open('volume','r')
unit_cell = f.read()

no_S_atoms = 2 #number of anions in the structure
cell_volume = float(unit_cell)*no_S_atoms
side = cell_volume**(1.0/3.0)

#For T2, x=0, y=side/2, and z = side/4
x=0
y=side/4
z=side/2

anion = bulk('S','bcc',a=side,covera=1,cubic=1) # 'S' can be changed to a different element
cation = Atom('Li',[x,y,z]) # 'Li' can be changed to a different element
atoms = anion + cation #building the structure

write('POSCAR',atoms,format='vasp') #writing the structure to a VASP file

#setting calculation parameters
calc = Vasp(    xc='PBE',
            encut=500,
            ibrion=2,
            npar=4,
            kpts=(6,6,6),
            ismear=-5,
            ispin=2,
            algo='Conjugate',
            ediffg=-0.2,
            nsw=0)

calc.initialize(atoms)
atoms.set_calculator(calc)
calc.write_incar(atoms) #writes INCAR file
calc.write_kpoints() #writes KPOINTS file

os.system('sbatch submit.sh')
```

DFT Python script for an uncharged Li-S FCC system with Li in the T1 position

```
from ase.io import write
from ase.build import bulk
from ase import Atom
from ase.calculators.vasp import Vasp
import os

os.system('cp ../volume .')
f = open('volume','r')
unit_cell = f.read()

no_S_atoms = 4
cell_volume = float(unit_cell)*no_S_atoms
side = cell_volume**(1.0/3.0)

# For O1, x=y=z=side/2
# For T2, x= y=z=side/4
x=side/4
y=side/4
z=3*side/4

anion = bulk('S','fcc',a=side,covera=1,cubic=1)
cation = Atom('Li',[x,y,z])

atoms = anion + cation

write('POSCAR',atoms,format='vasp')

calc = Vasp(    xc='PBE',
            encut=500,
            ibrion=2,
            npar=4,
            kpts=(6,6,6),
            ismear=-5,
            ispin=2,
            algo='Conjugate',
            ediffg=-0.2,
            nsw=0)

calc.initialize(atoms)
atoms.set_calculator(calc)
calc.write_incar(atoms)
calc.write_kpoints()

os.system('sbatch submit.sh')
```

DFT Python script for an uncharged Li-S HCP system with Li in the T1 position

```
from ase.io import write
from ase.build import hcp0001
from ase import Atoms
from ase.calculators.vasp import Vasp
import os
import math
from ase.io.vasp import write_vasp

os.system('cp ../volume .')
f = open('volume','r')

A = (float(f.read())*(2.0)**(1.0/2.0))**(1.0/3.0)

S = hcp0001('S',size=(2,2,3),a=A,orthogonal=True)
Li = Atoms('Li')

cell1 = S.get_cell()
cell1[2][2] = S.get_positions()[-1][2]
S.set_cell(cell1)
del S[[8,9,10,11]]

# For T2, Li.set_positions([(S.get_positions()[1]+S.get_positions()[2]+S.get_positions()[5]+
# S.get_positions()[3])/4])
# For T3, Li.set_positions([(S.get_positions()[10]+S.get_positions()[4]+S.get_positions()[5]+
# S.get_positions()[6])/4])
# For O1, Li.set_positions([(S.get_positions()[0]+S.get_positions()[5])/2])
# For O2, Li.set_positions([(S.get_positions()[8]+S.get_positions()[5])/2])

Li.set_positions([(S.get_positions()[2]+S.get_positions()[4]+S.get_positions()[5]+S.get_positi
ons()[6])/4])
atoms = S + Li

k1 = math.ceil(20/(cell1[0][0]))
k2 = math.ceil(20/(cell1[1][1]))
k3 = math.ceil(20/(cell1[2][2]))

write('POSCAR',atoms,format='vasp')

calc = Vasp(    xc='PBE',
            encut=500,
            ibrion=2,
            npar=4,
            kpts=(k1,k2,k3),
            ismear=-5,
            ispin=2,
            algo='Conjugate',
```

```
            ediffg=-0.2,
            nsw=0)

calc.initialize(atoms)
atoms.set_calculator(calc)
calc.write_incar(atoms)
calc.write_kpoints()

write_vasp('POSCAR',
        calc.atoms_sorted,
        symbol_count=calc.symbol_count)
calc.write_sort_file()


os.system('sbatch submit.sh')
```

INCAR parameters for DFT calculations on a charged BCC system

```
INCAR created by Atomic Simulation Environment
    ENCUT = 500.000000
    NELECT = 13.000000
    SIGMA = 0.100000
    EDIFFG = -2.00e-01
    GGA = PE
    NPAR = 4
    IBRION = 2
    NBANDS = 24
    NSW = 500
```

INCAR parameters for DFT calculations on a charged FCC system

```
INCAR created by Atomic Simulation Environment
    ENCUT = 500.000000
    NELECT = 25.000000
    SIGMA = 0.100000
    EDIFFG = -2.00e-01
    GGA = PE
    NPAR = 4
    IBRION = 2
    NBANDS = 32
    NSW = 500
```

INCAR parameters for DFT calculations on a charged HCP system

```
INCAR created by Atomic Simulation Environment
    ENCUT = 500.000000
    NELECT = 49.000000
```

```
SIGMA = 0.100000
EDIFFG = -2.00e-01
GGA = PE
ALGO = Conjugate
NPAR = 4
NELM = 200
IBRION = 2
NBANDS = 64
NSW = 500
```

Low Precision NEB calculation for a charged BCC system

```
import os

script = '''#!/usr/bin/env python

#SBATCH -p batch
#SBATCH -o myMPI.o%j
#SBATCH -N 1 -n 27
#SBATCH -t 48:00:00
#SBATCH --mail-type=END
#SBATCH --mail-user=aewang@uh.edu

# Number of nodes = number of images not including the initial and final states
import os
from ase.io import read
from ase.calculators.vasp import Vasp
import shutil

# Change according to system
os.environ['VASP_COMMAND']='mpirun vasp_std'

calc = Vasp(xc='PBE',
        ismear=-5,
        ispin=2,
        images=9,   #Enter the number of images
        npar=4,      # Change according to the system
        kpts=(6,6,6),
        encut=400,
        ediffg=-0.1,
        nsw=10000,
        nelect=13, # 25 for FCC; 49 for HCP
        nbands=24, # 32 for FCC, omit for HCP
        ibrion=3,
        spring=-5,
        potim=0.0,
        prec='Normal',
```

```
            ichain=0,
            iopt=3,
            algo='Conjugate',
            lwave=True,
            lcharg=False,
            lreal='False',
            lclimb=False)

atoms = read('./01/POSCAR')
atoms.set_calculator(calc)
atoms.get_potential_energy()
'''

wd = os.getcwd()
with open(wd+'/filename-low-prec', 'w') as f:
    f.write(script)
os.system('sbatch filename-low-prec')
os.chdir(wd)
```

High Precision NEB calculation for a charged BCC system

```
import os

script = '''#!/usr/bin/env python

# Change according to system
# Number of nodes = number of images not including the initial and final states
#SBATCH -p batch
#SBATCH -o myMPI.o%j
#SBATCH -N 1 -n 27
#SBATCH -t 48:00:00
#SBATCH --mail-type=END
#SBATCH --mail-user=aewang@uh.edu

from ase.io import read
from ase.calculators.vasp import Vasp
import shutil
import os, glob

cwd = os.getcwd()
imagedirs = glob.glob('0?')
imagedirs.sort()

for imagedir in imagedirs[1:-1]:
    os.chdir(imagedir)
    os.system('cat POSCAR > POSCAR.old')
    os.system('cat OUTCAR > OUTCAR.old')
```

```
    os.system('cat CONTCAR > POSCAR')
    os.chdir(cwd)

# Change accordingly
os.environ['VASP_COMMAND']='mpirun vasp_std'

calc = Vasp(xc='PBE',
            nsw=10000,
            ibrion=3,
            spring=-5,
            sigma=0.1,
            potim=0.0,
            prec='Normal',
            ichain=0,
            iopt=3,
            timestep=0.05,
            maxmove=0.05,
            algo='Fast',
            images=9,
            npar=4,
            lwave=False,
            lcharg=False,
            lreal='False',
            nelect=13, # 25 for FCC, 49 for HCP
            nbands=24, # 32 for FCC
            kpts=(6,6,6),
            encut=540,
            ediffg=-0.05,
            lclimb=True)

atoms = read('01/POSCAR')
atoms.set_calculator(calc)
atoms.get_potential_energy()
'''

wd = '.'
with open(wd+'/filename-high-prec', 'w') as f:
    f.write(script)

os.chdir(wd)
```